Mira, Maria; Olioso, Albert; Gallego-Elvira, Belen; Courault, Dominique; Garrigues, Sebastien; Marloie, Olivier; Hagolle, Olivier; Guillevic, Pierre; Boulet, Gilles. 2016. **Uncertainty assessment of surface net radiation derived from Landsat images.**

*Revised Manuscript with no Changes Highlighted

Uncertainty assessment of surface net radiation derived from Landsat images

Maria Mira[1,2,3], Albert Olioso[1,2], Belén Gallego-Elvira[4], Dominique Courault[1,2], Sébastien Garrigues[1,2], Olivier Marloie[5], Olivier Hagolle[6], Pierre Guillevic[7] and Gilles Boulet[6]

[(1)] INRA (French National Institute for Agricultural Research), UMR 1114 EMMAH, 84914 Avignon cedex 9, France

[(2)] UAPV (Université d'Avignon et des Pays de Vaucluse), UMR 1114 EMMAH, 84000 Avignon, France

[(3)] Grumets research group, Department of Geography, Universitat Autònoma de Barcelona (UAB), 08193 Bellaterra, Catalonia, Spain

[(4)] NERC Centre for Ecology and Hydrology, Wallingford, Oxfordshire OX10 8BB, United Kingdom

[(5)] INRA (French National Institute for Agricultural Research), UR 0629 URFM, 84914 Avignon, France

[(6)] CESBIO, BPI 811, 18 Avenue E. Berlin, 31401 Toulouse Cedex 9, France

[(7)] Jet Propulsion Laboratory, California Institute of Technology, 4800 Oak Grove Drive, Pasadena, CA 91109

Maria.Mira@uab.cat

ABSTRACT

The net radiation flux available at the Earth's surface drives evapotranspiration, photosynthesis and other physical and biological processes. The only cost-effective way to capture its spatial and temporal variability at regional and global scales is remote sensing. However, the accuracy of net radiation derived from remote sensing data has been evaluated up to now over a limited number of *in situ* measurements and ecosystems. This study aims at evaluating estimates and uncertainties on net radiation derived from Landsat-7 images depending on reliability of the input surface variables albedo, emissivity and surface temperature. The later includes the reliability of remote sensing information (spectral reflectances and top of canopy brightness temperature) and shortwave and longwave incoming radiations.

Primary information describing the surface is derived from remote sensing observations. Surface albedo is estimated from spectral reflectances using a narrow-to-broadband conversion method. Land surface temperature is retrieved from top of canopy brightness temperature by accounting for land surface emissivity and reflection of atmospheric radiation; and emissivity is estimated using a relationship with a vegetation index and a spectral database of soil and plant canopy properties in the study area. The net radiation uncertainty is assessed using comparison with ground measurements over the Crau-Camargue and lower Rhone valley regions in France. We found Root Mean Square Errors between retrievals and field measurements of 0.25–0.33 (14–19 %) for albedo, ~1.7 K for surface temperature and ~20 Wm^{-2} (5 %) for net radiation. Results show a substantial underestimation of Landsat-7 albedo (up to 0.024), particularly for estimates retrieved using the middle infrared, which could be due to different sources: the calibration of field sensors, the correction of radiometric signals from Landsat-7 or the differences in spectral bands with the sensors for which the models where originally derived, or the atmospheric corrections. We report a global uncertainty in net radiation of 40–100 Wm^{-2} equally distributed over the shortwave and longwave radiation, which varies spatially and temporally depending on the land use and the time of year. *In situ* measurements of incoming shortwave and longwave radiation contribute the most to uncertainty in net radiation (10–40 Wm^{-2} and 20–30 Wm^{-2}, respectively), followed by uncertainties in albedo (<25 Wm^{-2}) and surface temperature (~8 Wm^{-2}). For the latter, the main factors were the uncertainties in top of canopy reflectances (<10 Wm^{-2}) and brightness temperature (5–7 Wm^{-2}). The generalization of these results to other sensors and study regions could be considered, except for the emissivity if prior knowledge on its characterization is not available.

Keywords: uncertainty analysis, net radiation, surface temperature, albedo, emissivity, Landsat, regional scale, temporal course

1. Introduction

Accurate characterization of the land surface energy balance is fundamental in climate studies for understanding the partitioning of energy and water at the Earth surface. It is also required at finer scales for evapotranspiration monitoring in irrigation management and water resources planning. Net radiation is the main driver of surface energy balance and evapotranspiration. It expresses the balance of radiative energy at the Earth surface and thus the available energy for exchanges of sensible and latent heat fluxes between the surface and the atmosphere. Net radiation (*Rn*) depends on several land surface parameters and variables, including surface albedo (α), surface emissivity (ε) and surface temperature (Ts) which are changing in space and time under the influences of the type of land use, water availability and incoming radiation. At the instantaneous scale, net radiation can be expressed as:

$$Rn = (1 - \alpha)R_{SW}{}^{\downarrow} + \varepsilon \left(R_{LW}{}^{\downarrow} - \sigma\, Ts^4\right) \quad (1)$$

where σ is the Stefan-Boltzmann constant, $R_{SW}{}^{\downarrow}$ the solar irradiance (or incoming shortwave irradiance), and $R_{LW}{}^{\downarrow}$ the atmospheric irradiance (or incoming longwave irradiance).

Remote sensing is the only methodology which makes it possible to assess the spatial distribution of land surface variables at regional scale in a cost-effective way. The main sensors which were available in the last decades for assessing energy balance at a relatively fine spatial resolution (~100 m) and on an operational basis were Thematic Mapper (TM) and Enhanced Thematic Mapper Plus (ETM+) on board of the Landsat satellites 5 and 7. As these sensors were in flight for long periods of time (Landsat 5 for almost 29 years and Landsat 7 for 14 years), they may be used to assess the impact of evolution in land use and climate on net radiation and surface energy balance. The scientific community has recognized the potential interest of the follow-up of Landsat missions (see Anderson et al. (2012)). The development of new satellite systems with improved performances, in particular in the thermal infrared bands, either in terms of radiometric resolution and accuracy, spatial resolution and revisiting time are also undergoing, for instance HyspIRI (Abrams and Hook 2013), MISTIGRI (Lagouarde et al. 2013) or THIRSTY (Crebassol et al. 2014). In parallel, there is an increased interest in the development of standardized remote sensing products that facilitate the use of remote sensing data for the various user communities. This is already well developed for low resolution sensors with products such as surface temperature, surface spectral reflectances, albedo, or Leaf Area Index (*e.g.*, for Moderate-Resolution Imaging Spectroradiometer (MODIS), SPOT-VEGETATION or PROBA-V sensors). The use of these products has made it possible strong progresses in global water and carbon cycle studies and monitoring the impact of recent climate evolutions over land (*e.g.*, Ciais et al. (2005), Tang et al. (2014), Xia et al. (2014)). The development of similar products for Earth Observation satellites at higher resolution is in project with the supply of new services for distributing ready-to-use information to the user community. Evidence of this is a data center dedicated to land surfaces named THEIA which has started to operate in 2014 in France (Hagolle et al. 2015; WWW1). It is a French national inter-agency organization designed to foster the use of images coming from the space observation of land surfaces. Within the Land Data Centre, the French Space Agency CNES set up a production center named MUSCATE (WWW2) which aims to provide operational products derived from time series of images acquired by Landsat, SPOT and Formosat-2 and later by the future satellites Sentinel-2 and Venµs (L'Helguen et al. (2014); Leroy et al. (2014); Hagolle et al. (2015)). Concerning Landsat, the data presently available consist in Top Of Canopy (TOC) spectral reflectances, together with a cloud mask, and Top Of Atmosphere (TOA) brightness temperatures. Work is undergoing for the production of TOC brightness temperature and surface temperature (Rivalland et al. 2014).

The main advantages of using land surface products result from *1)* the availability of information that can be used in applications without requiring a strong expertise in the preprocessing of remote sensing images (*e.g.*, georeferencing, atmospheric corrections and retrieval of biophysical variables), *2)* the standardization of data processing and data quality management, *3)* the improvement in data documentation and metadata, and *4)* the community use of the data which enhances feedback on their quality and use. It is important that the definition of land surface products takes into account the user needs in order to provide higher level of requirement definition and feedbacks.

The accuracy of surface net radiation information derived from remote sensing data has been evaluated, in particular in the frame of evapotranspiration estimation and mapping. Root Mean Square Errors (*RMSE*) between remote sensing retrievals and field data were found typically in a 20 to 80 Wm^{-2} range (*e.g.*, Jacob et al. (2002a); Tang et al. (2011); Merlin et al. (2014); Wang et al. (2014)). However, these analyses compared remote estimates to a limited number of *in situ* measurements over specific ecosystems. Few studies have dealt with the impact of uncertainties in the derivation of the surface variables required to map surface net radiation products and associated uncertainties (*e.g.*, Bhattacharya et al. (2010); Tang et al. (2011); Cheng et al. (2013); Mattar et al. (2014)). The performance of the algorithms used to estimate variables in order to derive net radiation, such as albedo, surface temperature and emissivity needs to be evaluated.

The objective of this study is to assess the uncertainties in surface net radiation estimates due to uncertainties in the derivation of surface albedo, surface emissivity and surface temperature from pre-operational remote sensing products, as well as uncertainties in atmospheric information and incoming radiations. We focused on the derivation of albedo, emissivity and surface temperature from Landsat-7 products provided by the THEIA Land Data Centre. The analysis was performed over the lower Rhône Valley region, South Eastern France, where a dense network of ground stations measuring surface energy balance components and meteorological variables was set up on various surfaces for several years. The methodology and data are presented in Section 2. Results are presented in Section 3 and discussed in Section 4, respectively.

2. Materials and methods

2.1. Background and definitions

Surface albedo is a dimensionless characteristic of the soil-plant canopy system which represents the fraction of solar energy reflected by the surface. It is expressed as the ratio of the radiant energy scattered upward by a surface in all directions, compared to that received from all directions, integrated over the wavelengths of the solar spectrum (Pinty and Verstraete 1992). Sellers et al. (1995) suggested that an absolute accuracy of 0.02 is required for climate modeling. The latter corresponds to a typical accuracy on monthly averaged reflected solar irradiance at the satellite overpass of 10 Wm^{-2}. It is expected that the estimation of albedo from multispectral remote sensing can reach these requirements. When considering instantaneous flux, a simple calculation shows that an absolute accuracy of 0.02 (roughly equivalent to 10 % error in albedo for agricultural landscape) corresponds to a relative accuracy on net radiation of around 5 %. As shown in Jacob et al. (2002a) in the context of mapping evapotranspiration, this accuracy may result in an absolute error of 20 Wm^{-2} in net radiation (*RMSE* established over 16 days with remote sensing acquisition over 6 months and 3 to 5 ground measurements of net radiation).

The most classical approach to derive albedo from multispectral remote sensing is the Narrow-To-Broadband (NTB) conversion method (*e.g.*, Brest and Goward (1987); Ranson et al. (1991); Weiss et al. (1999); Liang (2000); Jacob et al. (2002b); Jacob et al. (2002c)). This method considers that it is possible to integrate the surface reflectance obtained in the spectral bands provided by visible – near infrared – middle infrared sensors through a linear combination to represent the whole solar domain.

Surface emissivity is defined as the ratio between the emission of the Earth surface and the emission of a black body at the same thermodynamic (or kinetic) temperature (Norman and Becker 1995). When considering the calculation of net radiation, the knowledge of emissivity over the whole spectral range of thermal radiation is required to compute emission of radiation from the surface (surface temperature term). In Eq. (1), the emissivity is also required for computing the absorption of atmospheric radiation. The equivalence between the coefficient of absorption and the emissivity considers that the Kirchhoff's law of thermal radiation applies, which supposes that the land surface is isothermal. The accuracy of emissivity is directly transmitted into the accuracy of the emission term in the net radiation equation, but this impact is partially cancelled out by the absorption term. An uncertainty of 0.1 in surface emissivity roughly corresponds to an uncertainty of 15 to 20 Wm^{-2} in net radiation (Ogawa and Schmugge 2004), which is in the same order as the uncertainty due to albedo presented above.

The derivation of surface emissivity from remote sensing is not straightforward. One possibility would be to map surface spectral emissivity from thermal infrared multispectral spectral sensors such as ASTER using for instance the Temperature and Emissivity Separation (TES) algorithm proposed by Gillespie et al. (1998), and then to convert the spectral values in a broadband emissivity using a NTB conversion method in a similar way to what is done to derive albedo. Ogawa and Schmugge (2004), confirmed by Cheng et al. (2013), showed that the best integration windows for representing surface emissivity for net radiation calculation would be the 8.0–13.5 µm spectral range. Since TM and ETM+ have only one thermal infrared band, it is not possible to obtain emissivity directly using methods such as the TES algorithm. An alternative method consists in using relationships with vegetation indices or reflectance measurements in the solar domain (Van de Griend and Owe (1993); Olioso (1995b); Valor and Caselles (1996); Wittich (1997); Sobrino et al. (2001); Olioso et al. (2007); Caselles et al. (2012)). These methods were originally designed for deriving the spectral emissivity required for estimating surface temperature from thermal measurements (see next paragraph), so that they would have to be recalibrated when dealing with the surface emissivity used in net radiation calculation.

<u>*Land surface temperature*</u> is closely related to the surface energy balance and to the water status of the surface. It mainly depends on the amount of radiative energy absorbed by the surface, on the partitioning of heat in sensible and latent heat flux, and on the characteristics of the atmosphere close to the ground (in particular air temperature and turbulence). Surface temperature can be derived from thermal infrared measurements. For energy balance studies an accuracy better than 1 K is required for achieving an overall accuracy on instantaneous heat flux better than 50 Wm^{-2} (Norman et al. 1995; Seguin et al. 1999). However this requirement is mainly driven by the estimation of heat fluxes rather than net radiation. As a matter of fact an error of 1 K in surface temperature would result in an error around 6 Wm^{-2} for net radiation. From TM and ETM+ sensors, the possibility to reach this level of accuracy requires the knowledge of the emissivity of the surface in the spectral band of the sensor (which is different from the large band emissivity required in Eq.(1)). Olioso (1995a) showed that for a spectral emissivity of 0.94 in the TM band, errors up to 4 K or more, depending on the atmospheric conditions, would be obtained when not accounting for emissivity effect. Mira et al. (2007) observed that an emissivity variation of ±0.06 causes an error of ±2.2 K in the surface temperature determination (at 11 µm and for a temperature of 300 K). As for large band emissivity above, spectral emissivity can be estimated in the TM and ETM+ thermal bands from vegetation indices or reflectances measurements. These methods provide a practical way to estimate spectral emissivity of

natural surfaces with typical errors around 1 % to 2 %. The most classical approach which relates emissivity to the Normalized Difference Vegetation Index (*NDVI*) was first established experimentally by Van de Griend and Owe (1993). Olioso (1995b) and Olioso et al. (2007) used experimental data and radiative transfer modeling in vegetation canopy to explore the variability of the relationship between vegetation index and spectral emissivity. They showed that leaf optical properties and soil surface emissivity were the two main sources of uncertainty.

2.2. The experimental area

The study region is located in the lower Rhône Valley, South Eastern France, including the Avignon area (43.92° N; 4.88° E; 32 m above sea level) and the Crau-Camargue area (50 km around 43.56° N; 4.86° E; 0 to 60 m above sea level). It is mainly a flat area with very gentle slope (less than 0.5 %) which presents a wide variety of surfaces including dry and irrigated grasslands, wetlands and various crops (Fig. 1). Climate is Mediterranean, with irregular precipitations (annual cumulative precipitation range between 350 mm and 1100 mm with an average of 550 mm), long dry periods in spring and summer, and strong winds.

[Insert Fig. 1 about here]

The area is covered by a single Landsat-7 ETM+ image. A network of ground stations was deployed over different types of ecosystems representative of the main land use in the area (Fig. 1) to monitor surface energy balance and meteorological variables. Four stations were considered in this study. In order to avoid topography effects related to the hills present in the images, pixels with an elevation higher than 100 m were masked.

2.3. Mapping land surface variables from Landsat-7 ETM+ data

2.3.1. Landsat data

The ETM+ (on board of Landsat-7) acquires data following a Sun synchronous orbit with a revisit interval of 16 days since 1999. Since May 2003, only the central part of the scene is easily workable, with approximately 44 km swath available (Chander et al. 2009). ETM+ measures radiances in 7 spectral bands covering the solar and the thermal domains. Instantaneous fields of view of the sensor correspond to a spatial resolution at the ground of 30 m for bands 1 to 4 (visible to near infrared), 5 and 7 (middle infrared) and 60 m for band 6 (thermal infrared band).

Landsat data used in this study were provided as ready-to-use products by the production center named MUSCATE set up by CNES within THEIA (Hagolle et al. 2015; L'Helguen et al. 2014; WWW1). They consist in TOC spectral reflectances and TOA brightness temperatures. We also produced TOC brightness temperature as a prototyping phase of future products (Rivalland et al. 2014). The original data were downloaded from USGS (US Geological Survey) and then processed by MUSCATE. Images were corrected for geolocation, radiometric calibration and atmospheric effects according to the methods described by Baillarin et al. (2008) and Hagolle et al. (2008, 2010, 2015). Radiometric calibration was performed using the calibration coefficients provided by USGS (Chander et al. 2009). The calibration uncertainties of at-sensor spectral radiances are 5 % (Chander et al. 2009).

Atmospheric corrections in the solar domain, as well as the creation of masks for clouds, cloud’s shadows, water bodies and snow surfaces were performed using the Multi-sensor Atmospheric Correction and Cloud Screening (MACCS) (Hagolle et al. 2015) spectro-temporal processor used within the French THEIA Land Data Centre. The procedure to create masks combined the detection of a sudden increase of reflectance in the blue wavelength on a pixel by pixel basis, several spectral tests to check that the clouds are white in the visible, and a test of the linear correlation of pixel neighborhoods taken from couples of images acquired successively (Hagolle et al. 2010). The procedure was tuned to identify even thin clouds. It had a low amount of false detections even when the gap between two clear images increases to one or two months. The shadow detection also used a multi-temporal approach and classified as "potential shadows" the pixels for which a darkening of the surface in the red band was observed. The potential shadows were finally classified as shadows when a cloud was geometrically matched to the shadow. The atmospheric corrections in the solar domain were based on the inversion of an atmospheric radiative transfer model by exploiting the differential behavior of TOA reflectances in time and space depending on the variations in aerosol content of the atmosphere and the variations of surface properties. Hagolle et al. (2008), both with simulated and experimental data (Formosat-2 images), showed that the method worked well, in particular when the aerosol optical thickness varied significantly with time. This was particularly true over our area where aerosol optical thickness and surface reflectances were retrieved with a good accuracy. The adaptation of the method, originally designed for sensors with a revisit of only few days (as Formosat-2 or VENμS in the future), to ETM+ did not degrade the accuracy of the atmospheric correction significantly (Hagolle et al. (2012, 2015)). The inversion procedure and the atmospheric corrections were set accounting for the absorption by atmospheric molecules considering average values of ozone, oxygen and water vapor concentrations (Hagolle et al. 2008). A constant value of 3 cm was considered for the atmospheric precipitable water (W). Nevertheless, this estimate will improve with the use of meteorological data within the processing chain, expected for the new operational version next year.

TOC brightness temperatures (*Tb*) were produced from the TOA brightness temperatures after removing the atmospheric effect using the atmospheric radiative transfer model MODTRAN® (Berk et al. 2003). Atmospheric profiles of pressure, temperature and humidity required for running MODTRAN® were obtained from *in situ* radiosoundings launched at 12:00 UTC at Nîmes airport by Météo-France, located 30 km west of the study area. Radiosonde data were downloaded from (WWW3). TOC brightness temperatures were obtained by considering land surface emissivity equals to 1. Conversely to land surface temperature, TOC brightness temperature is not depending on any assumption on the definition of land surface emissivity. Thus, it can be used in a variety of applications including the assimilation in land surface models that generate thermal signals from coupled energy balance - radiative transfer parameterization (Olioso et al., 1999) or the evaluation of thermal infrared emission models such as the SCOPE model (Van der Tol et al., 2009; Duffour et al., 2015). In the present study, it was used to derive land surface temperature assuming specific estimations of land surface emissivity (see below).

In the present study, 27 Landsat-7 ETM+ images acquired at about 10:15 UTC between 2007 and 2010 were used (*i.e.*, around 7 images per year). The center of the images was targeted at nadir, while the viewing angle increases by about 7 or 8 degrees at the extreme of the workable part of the images. Solar zenith angle varied throughout the experimental period from 27º to 69º, depending on time of year.

2.3.2. Albedo estimation

We estimated albedo (α) from spectral reflectances (ρ_j) using the NTB conversion method:

$$\alpha = \beta_0 + \sum_{j=1}^{n} \beta_j . \rho_j \quad (2)$$

where subscript j refers to the spectral band number and n to the number of bands, β_j is the weighting coefficients, and β_0 is the offset. We considered thirteen coefficient sets from the literature that can be applied to ETM+ spectral bands. They were labeled as *m1–m13* and are summarized in Table 1. They were originally obtained by calibrating the linear combination model using either experimental data (*m1 to m7*), dataset simulated using radiative transfer models (*m8, m9, m11* to *m13*), or theoretical consideration on the representativity of each spectral band (*m10*) – see associated references in Table 1. Coefficient sets *m1* and *m4* to *m7* were obtained after calibration over datasets acquired in the same area as our study. Coefficient sets *m2*, *m3*, *m8* and *m10* were derived for TM or ETM+ sensors and included bands in the middle infrared. Other coefficient sets were derived for other sensors including Formosat-2, Airborne Polder, MISR, AVHRR, SEVIRI and MERIS. Formosat-2 had spectral bands very similar to ETM+, but not including middle infrared bands 5 and 7. Spectral bands for the other sensors may be significantly different from Landsat bands. Differences also occurred related to the geometry of spectral reflectance used when calibrating the linear model: hemispherical reflectances (*m7* to *m9, m11* to *m13*), bi-directional reflectances at nadir (*m2* to *m6, m10*) and off nadir (~40°) bi-directional reflectances (*m1*). Work by Jacob and Olioso (2002) showed that using nadir reflectances (*m4* to *m6*) instead of hemispherical reflectances (*m7*) to derive the linear model coefficients had an impact on the accuracy in albedo retrieval (~25 % increase in albedo calibration *RMSE*), while the model analysis performed by Bsaibes et al. (2009) showed that the zenith viewing angle was not affecting the derivation of the β_j coefficients.

[Insert Table 1 about here]

2.3.3. Surface temperature estimation

Land surface temperature (*Ts*) was computed from TOC brightness temperature (*Tb*) by accounting for land surface emissivity and reflection of atmospheric radiation according to the equation proposed by Olioso (1995a):

$$Ts - Tb_{\lambda_1-\lambda_2} \cong \frac{(1-\varepsilon_{\lambda_1-\lambda_2})}{4\,\varepsilon_{\lambda_1-\lambda_2}} Tb_{\lambda_1-\lambda_2} - \frac{(1-\varepsilon_{\lambda_1-\lambda_2})}{4\,\varepsilon_{\lambda_1-\lambda_2}\, f_{\lambda_1-\lambda_2}(Tb_{\lambda_1-\lambda_2})\sigma Tb_{\lambda_1-\lambda_2}{}^{3}} R_{LW}{}^{\downarrow}_{\lambda_1-\lambda_2} \qquad (3)$$

where subscript λ_1–λ_2 refers to the spectral band of the thermal infrared sensor. The first term is an 'emissivity term' which increases with the reflectivity of the surface ($1-\varepsilon_{\lambda 1-\lambda 2}$) and with the temperature. The second term is an 'atmospheric radiation term' which also increases with the surface reflectivity, but decreases with the temperature, and is proportional to the atmospheric radiation. Factor $f_{\lambda 1-\lambda 2}(T)$ corresponds to the fraction of energy emitted in the considered spectral domain by a black body at temperature *T* relative to the emitted energy over the full spectrum. When considering ETM+ band 6, the following formulation is given by Idso (1981) (originally from Harrison (1960)):

$$f_{10.4-12.5\,\mu m}(T) = -0.2338 + 0.2288 \cdot 10^{-2}\,T - 0.3617 \cdot 10^{-5} T^2 \qquad (4)$$

$f_{10.4-12.5\,\mu m}(T)$ varies between 0.12 and 0.13 for temperatures between -10 ºC and +45 ºC. In the 10.4–12.5 µm range, the incoming atmospheric radiation ($R_{LW}{}^{\downarrow}{}_{10.4-12.5\,\mu m}$) was expressed as a function of air temperature and a spectral atmospheric emissivity ($\varepsilon_{a\ 10.4-12.5\,\mu m}$) as given by Idso (1981):

$$R_{LW}{}^{\downarrow}_{10.4-12.5\ \mu m} = \varepsilon_{a\ 10.4-12.5\ \mu m} \cdot\ f_{10.4-12.5\ \mu m}(T_a) \cdot \sigma \cdot {T_a}^4 \tag{5}$$

Based on measurements in clear sky conditions, Idso (1981) expressed $\varepsilon_{a\ 10.4–12.5\ \mu m}$ as a function of air temperature T_a (K) and air water vapor pressure e_a (mbar) at surface level. Actually, emissivities used by Idso (1981) were derived from brightness sky temperature measurements made with an infrared thermometer facing the zenith ($T_{atm,0}$) and receiving radiation from approximately two degree viewing angle, assuming that:

$$R_{LW}{}^{\downarrow}_{10.4-12.5\ \mu m} = f_{10.4-12.5\ \mu m}\left(T_{atm,0}\right) \cdot \sigma \cdot {T_{atm,0}}^4 \tag{6}$$

However, the effective brightness temperature of the whole sky hemisphere cannot be characterized by a single temperature at zenith (Rubio et al. 1997), and a corrective factor ($\gamma_{10.4–12.5\ \mu m}$) should be included in Eq. (6) such as:

$$R_{LW}{}^{\downarrow}_{10.4-12.5\ \mu m} = \gamma_{10.4-12.5\ \mu m} \cdot\ f_{10.4-12.5\ \mu m}\left(T_{atm,0}\right) \cdot \sigma \cdot {T_{atm,0}}^4 \tag{7}$$

Hence, the spectral atmospheric emissivity in the 10.4–12.5 µm range derived by Idso (1981) should be reformulated as:

$$\varepsilon_{a\ 10.4-12.5\ \mu m} = \gamma_{10.4-12.5\ \mu m} \cdot\ 5.91 \cdot 10^{-6} \cdot e_a \cdot exp\left(\frac{2450}{T_a}\right) \tag{8}$$

García-Santos et al. (2013), exploring a large range of environmental conditions, provided the basis for expressing $\gamma_{10.4–12.5\ \mu m}$ as a linear function of W. We assumed that $\gamma_{10.4–12.5\ \mu m}$ can be approximated as the average of similar γ factors calculated by García-Santos et al. (2013) in the two spectral bands 10.2–11.3 µm and 11.5–12.4 µm :

$$\gamma_{10.4-12.5\ \mu m} = 1.67 - 0.09\ W \tag{9}$$

In our study, W was obtained from the local-radiosonding profiles made at Nîmes airport. W ranged from 0.29 to 3.21 cm, causing $\gamma_{10.5–12.5\ \mu m}$ values ranging from 1.38 (for the wettest atmosphere) to 1.64 (for the driest). These coefficients imply to increase significantly the original values of atmospheric emissivity from Idso (1981) study (which ranged from 0.1 (dryer cases) to 0.6 (wetter cases)).

2.3.4. Emissivity estimation

Land surface emissivities were required to convert TOC brightness temperature to land surface temperature and for the computation of net radiation: respectively spectral emissivity in the ETM+ band 6 (10.4 – 12.5 µm) and emissivity in the 8.0 – 13.5 µm range. Wittich (1997) proposed a simple analysis that made it possible to derive emissivity using a simple and generic formula from the *NDVI*:

$$\varepsilon_{\lambda_1-\lambda_2} = \varepsilon_{\infty\,\lambda_1-\lambda_2} - \left(\varepsilon_{\infty\,\lambda_1-\lambda_2} - \varepsilon_{s\,\lambda_1-\lambda_2}\right)\left(\frac{NDVI-NDVI_{\infty}}{NDVI_s-NDVI_{\infty}}\right)^k \qquad (10)$$

The subscript *s* stands for bare soil conditions and the subscript ∞ for full vegetation canopy cover. *NDVI* is defined from near infrared (NIR) and red reflectances (band 4 and 3 on ETM+, respectively) as:

$$NDVI = \frac{\rho_{NIR}-\rho_{Red}}{\rho_{NIR}+\rho_{Red}} \qquad (11)$$

Eq. (10) can be applied to any study site as long as its coefficients (*k*, $\varepsilon_{s\,\lambda_1-\lambda_2}$, $\varepsilon_{\infty\,\lambda_1-\lambda_2}$, NDVIs and $NDVI_{\infty}$) can be derived from information on soil and plant canopy properties in the area of interest. Coefficient *k* mainly depends on the mean leaf inclination angle and the viewing angle. Simulation studies by Anton and Ross (1990), Olioso (1995b) and François et al. (1997) shown that *k* varies between 1 and 3.

Field measurements of emissivity were not performed in our area during the studied period, so that we derived $\varepsilon_{s\,\lambda_1-\lambda_2}$ and $\varepsilon_{\infty\,\lambda_1-\lambda_2}$ from data acquired over the same area during previous experiments, as well as data obtained over dense canopies of similar vegetation types in other sites. All these data are presented in Table 2. For bare soil we also considered laboratory measurements of reflectance spectra in the 0.4–14.0 μm domain at various soil moisture levels. They were performed by Lesaignoux et al. (2013) over samples collected over our experimental area in 2007 and 2008 (see Table 3). Band emissivities $\varepsilon_{\lambda_1-\lambda_2}$ were calculated considering the convolution of the reflectance spectra to the considered bands:

$$\varepsilon_{\lambda_1-\lambda_2} = \frac{\int_{\lambda_1}^{\lambda_2} S_\lambda^{'}(1-\rho_\lambda)\, B_\lambda(T)\, d\lambda}{\int_{\lambda_1}^{\lambda_2} S_\lambda^{'} B_\lambda(T)\, d\lambda} \qquad (12)$$

where $B_\lambda(T)$ is the Planck's function at temperature T (approximated as 300 K), ρ_λ is the soil spectral reflectance (which is used to compute the spectral emissivity as $\varepsilon_\lambda=1-\rho_\lambda$, according to Kirchhoff's law) and S_λ' is the normalized spectral response function of band λ_1–λ_2. Similarly, $NDVI_s$ was derived from early mentioned spectral signatures of the 21 bare soils measured by Lesaignoux et al. (2013) and compared with values from our ETM+ images. $NDVI_\infty$ was approximated to 0.90 in agreement with maximum values from the images.

[Insert Table 2 about here]

[Insert Table 3 about here]

2.3.5. Net radiation estimation

Net radiation maps were computed using Eq. (1) using maps of albedo, land surface temperature and emissivity derived from Landsat radiances. Incoming radiations were obtained from the INRA meteorological station network over the area combined to the four energy balance stations used in this study (see below). Incoming irradiances $R_{SW}^{\downarrow}$ and $R_{LW}^{\downarrow}$ and air vapor pressure and temperature e_a and T_a (required for calculating the incoming atmospheric radiation in the 10.4–12.5 μm range, $R_{LW}^{\downarrow}{}_{10.4-12.5\,\mu m}$) were spatially interpolated by inverse distance weighting. Spatial variations were not remarkable for air temperature and vapor pressure (maximum differences of 4 hPa for e_a, 1.7 K for T_a). For incident radiations, spatial variations were usually low, but reached higher values for very few dates (maximum differences of 76 Wm^{-2} for $R_{SW}^{\downarrow}$, 28 Wm^{-2} for $R_{LW}^{\downarrow}$).

2.4. Ground based measurements for net radiation, albedo and surface temperature assessments

Ground measurements were performed at four experimental sites (see Fig. 1) located in lower Rhone region (*Avignon site*) and la Crau-Camargue region (*Coussouls*, *Domaine du Merle* and *Tour du Valat sites*) in France:

(1) The *Avignon site* consisted in a 2 ha field located in a semi-urban area. A succession of arable crops was cultivated from 2007 to 2010: sorghum, wheat, corn, sorghum and wheat. A full description of the site and data is given by Garrigues et al. (2014).

(2) The *Coussouls site* corresponded to a large and flat stony area of more than 7400 ha at the center of the Crau area. It was covered by a specific dry grass ecosystem (locally named 'coussouls'). In spring, the 'grass' was grazed by sheep; in summer, the vegetation dried out quickly.

(3) The *Domaine du Merle site* consisted in a 4.5 ha of irrigated meadows surrounded by other irrigated meadows in the North of the Crau area. It was irrigated by flooding every 11 days from March to September. Three cuts were performed during the growing season (May, July and September) and it was grazed by sheep in winter.

(4) The *Tour du Valat site* was located in Camargue over a Mediterranean saltmarsh scrubs area (locally known as 'sansouires'), mostly composed of halophytic vegetation such

as *Salicornia sp.* and *Arthrocnemion sp.* The vegetation distribution was heterogeneous at fine scale, creating surfaces presenting more or less large bare soil patches dotted with dense vegetation spots. A full description of the site is given by Gallego-Elvira et al. (2013).

Net radiation, albedo and surface brightness temperature were measured in the four stations considered in this study. Measurements started in 2000 in *Avignon (site 1)*, in 2007 in *Tour du Valat (site 4),* in 2008 in *Domaine du Merle (site 3)*, and in 2010 in *Coussouls (site 2)*. CNR1 net radiometers (Kipp & Zonen, Delft, The Netherlands) were used, except for *site 1* after September 2009 where a CNR4 net radiometer was installed. Description of the instruments can be found in Kohsiek et al. (2007) and at the manufacturer website (WWW4). CNR1 were composed of a CM3 pyranometer (0.3–2.8 µm) and a CG3 pyrgeometer (5–42 µm) pair that faced upward and a complementary pair that faced downward. They measured the radiative balance terms including incoming ($^{\downarrow}$) and outgoing ($^{\uparrow}$) irradiances in the solar domain (global radiation R_{SW}) and the thermal infrared domain (atmospheric radiation R_{LW}). The instruments were mounted between 1.5 m and 2 m above canopy top. Radius of the measurement footprint ranged from 25 to 35 m. The measurements were made every second and averaged every 30 minutes. In *site 1* solar irradiance was also measured by higher quality instruments, an Eppley Precision Spectral Pyranometer PSP (0.3–2.8 µm) (EPLAB, Rhode Island, USA; (WWW5)) or a CMP21 (0.3–2.8 µm; manufactured by Kipp & Zonen, Delft, The Netherlands).

We calibrated CM3 and CG3 sensors on an annual basis along the measurement period following the process described in documents from International Organization for Standardization (ISO 1992) and World Meteorological Organization (WMO 2008). Sensors were compared at *site 1* to reference radiation sensors (CMP21 and CG4 sensors) linked to the radiation reference at the World Radiation Center in Davos (Switzerland) through Météo-France calibration facilities in Carpentras (France). Estimated uncertainties, combined and expanded (95 %), lower than 5 % and 8 % were obtained for the sensitivity of CM3 pyranometer and CG3 pyrgeometer, respectively. This uncertainty was calculated as the root square sum of uncertainties of random effects during outdoor comparison, datalogger voltages, sensitivity of reference sensor and instrument temperature measurements for CG3 and reference pyrgeometer.

Net radiation (Rn) was calculated from the irradiances measured by the four components of the CNR1 net radiometer following:

$$Rn = R_{SW}{}^{\downarrow} - R_{SW}{}^{\uparrow} + R_{LW}{}^{\downarrow} - R_{LW}{}^{\uparrow} \tag{13}$$

Albedo (α) was obtained as the ratio of the irradiance corresponding to the reflected solar radiation to the incoming irradiance (from CM3, CMP21 or PSP sensors):

$$\alpha = \frac{R_{SW}{}^{\uparrow}}{R_{SW}{}^{\downarrow}} \tag{14}$$

Surface temperature was computed from the outgoing thermal irradiance ($R_{LW}{}^{\uparrow}$) based on the Stefan-Boltzmann law and the application of Eq. (3) for the 5–50 μm spectral range (Eq. 15 and 16).

$$Ts - Tb_{5-50\,\mu m} \cong \frac{(1-\varepsilon_{8.0-13.5\,\mu m})}{4\,\varepsilon_{8.0-13.5\,\mu m}} Tb_{5-50\,\mu m} - \frac{(1-\varepsilon_{8.0-13.5\,\mu m})}{4\,\varepsilon_{8.0-13.5\,\mu m}\,\sigma Tb_{5-50\,\mu m}{}^{3}} R_{LW}{}^{\downarrow} \tag{15}$$

$$Tb_{5-50\,\mu m} = \left(\frac{R_{LW}{}^{\uparrow}}{\sigma}\right)^{1/4} \tag{16}$$

with $Tb_{5\text{–}50\ \mu m}$ the brightness temperature (K). Note that in the spectral range considered here, the factor $f_{5\text{–}50\ \mu m}$ in Eq. (3) corresponded to unity and that the surface emissivity was assumed to be obtained in the 8.0–13.5 μm spectral range (following Ogawa and Schmugge

(2004) and Cheng et al. (2013)). Emissivities $\varepsilon_{8.0\text{-}13.5\mu m}$ were estimated from ground information on canopy cover and database information on soil emissivity and canopy emissivity (Table 2 and Table 3).

2.5. Performance metrics

In order to measure the performance of remote sensing estimates (*i.e.*, *Rn*, *α* and *Ts*), standards metrics were analyzed. The Mean Error (*ME*) is the bias between estimated values ($Estim_i$) and ground-based measurements ($Meas_i$):

$$ME = \frac{1}{N}\sum_{i=1}^{N}(Estim_i - Meas_i) \quad (17)$$

where *N* is the number of samples. The estimated data ($Estim_i$) correspond to the average over a 3×3 pixels window centered at the station. Standard deviations of the estimated values were providing information on the spatial heterogeneity around the field station. Absolute and Relative Root Mean Square Error ($RMSE_A$ and $RMSE_R$, respectively) quantified the scatter between measured and estimated values, leading to a quantitative assessment of the accuracy and precision of our estimates:

$$RMSE_A = \sqrt{\frac{1}{N}\sum_{i=1}^{N}(Estim_i - Meas_i)^2} \quad (18)$$

$$RMSE_R(\%) = \frac{RMSE_A}{mean(Meas_i)}100 \quad (19)$$

2.6. Evaluation of uncertainties

After characterizing the errors using the metrics above, we analyzed uncertainties. Uncertainty (hereafter specified by *δ*) gives a range of values likely to enclose the true value, while errors are directly derived from the difference between the estimates and the reference values. Therefore, the uncertainty concept is larger since it addresses error from all possible effects together. It can be assessed by different techniques (ex. Crosetto et al. (2001)). In our study, a simple approach was considered to assess the uncertainties in net radiation by considering the impact of the uncertainties in the remote sensing information (spectral reflectances and TOC brightness temperature), the incoming radiations (shortwave and longwave irradiance) and the derivation of the surface variables from remote sensing data (albedo, emissivity and surface temperature). We estimated uncertainties for each pixel and each day by considering half the maximum variation of the estimate (*A*) provided:

- by different models (M_1 to M_n) for related input variables following:

$$\delta A = \frac{max(A_{M_1\ to\ M_n}) - min(A_{M_1\ to\ M_n})}{2} \quad (20)$$

- or by the considered uncertainty of measurements (δx) following:

$$\delta A = \frac{abs[A(x+\delta x) - A(x-\delta x)]}{2} \quad (21)$$

Uncertainty in net radiation due to uncertainty in incoming shortwave ($\delta R_{SW}{}^{\downarrow}$) and longwave ($\delta R_{LW}{}^{\downarrow}$) radiation was calculated following Eq. (21) as:

$$\delta Rn(R_{SW}{}^{\downarrow}) = (1 - \alpha) \cdot \delta R_{SW}{}^{\downarrow} \quad (22)$$

$$\delta Rn(R_{LW}{}^{\downarrow}) = \varepsilon \cdot \delta R_{LW}{}^{\downarrow} \quad (23)$$

Uncertainties of 5 % and 8 % (see Section 2.4) were considered for $R_{SW}{}^{\downarrow}$ and $R_{LW}{}^{\downarrow}$ to account for their spatial heterogeneity and instrument calibration (*e.g.*, $\delta R_{SW}{}^{\downarrow}=0.05 \cdot R_{SW}{}^{\downarrow}$ and $\delta R_{LW}{}^{\downarrow}=0.08 \cdot R_{LW}{}^{\downarrow}$). These calculations of net radiation uncertainties considered the impact of uncertainties in incoming radiations alone.

Uncertainty in net radiation due to uncertainty in spectral reflectances from satellite sensor ($\delta\rho_i$) was estimated following:

$$\delta Rn(\rho_i) = Rg^{\downarrow} \cdot \sum_i^n \beta_i \cdot \delta\rho_i \quad (24)$$

where βi were the coefficients of the albedo model. Relative uncertainties of 5 % were assumed for each spectral band, equivalent to the calibration uncertainties according to Chander et al. (2009), while it could be considered greater due to atmospheric correction process and depending on the wavelength.

Uncertainty in net radiation due to uncertainty in TOC brightness temperatures (δTb) was calculated following:

$$\delta Rn(Tb) = \varepsilon_{8.0-13.5\mu m} \cdot \sigma \cdot \frac{abs[\,Ts(Tb+\delta Tb)^4 - Ts(Tb-\delta Tb)^4]}{2} \qquad (25)$$

We considered δTb equal to 1 K. This uncertainty level was in agreement with the analyses for monospectral sensors by Jacob et al. (2003), Li et al. (2004) and Mira et al. (2014) in relation to the spatial and temporal representativity of atmospheric information used for atmospheric corrections (*i.e.*, spatial location and time of atmospheric profiles of temperature and humidity, and influence of the local atmospheric conditions in the lower layer of the atmosphere).

Uncertainty in net radiation due to uncertainty in albedo $\delta\alpha$ was derived following Eq. (20) as follows:

$$\delta Rn(\alpha) = \delta\alpha \cdot R_{SW}{}^{\downarrow} \qquad (26)$$

$$\delta\alpha = \frac{max(\alpha_{m_1\, to\, m_n}) - min(\alpha_{m_1\, to\, m_n})}{2} \qquad (27)$$

where m_i stands for the different albedo models considered for the analysis: $i = 1$ to 13 when considering all the albedo models; $i = 2, 3, 8, 10$ when considering only models established for Landsat images; $i = 1, 2, 3, 8, 10$ when considering Formosat-2 data together with Landsat data, as Formosat-2 wavebands are very similar to ETM+ bands 1 to 4. In these calculations, only albedo uncertainty was accounted for.

The impact of uncertainties in land surface emissivity ($\varepsilon_{8.0\text{-}13.5\mu m}$) was evaluated in a similar way as for albedo by considering different estimates (these different estimates are presented in the results section).

Uncertainty in net radiation due to uncertainties in land surface temperature retrievals depends on uncertainties in land surface emissivity $\varepsilon_{10.4\text{-}12.5\mu m}$ and incoming atmospheric radiation $R_{LW}{}^{\downarrow}{}_{10.4\text{-}12.5\mu m}$. Uncertainties of brightness temperature due to calibration process are not accounted for in the analysis. The calculations were done by considering either both variables independently or combined. Estimations of incoming radiation were evaluated from the combined variation of e_a and T_a over the various meteorological stations and different W estimates from the radiosoundings and the National Centers for Environmental Prediction (NCEP) profiles provided by (WWW6).

Global uncertainties of surface net radiation, as well as uncertainties of shortwave and longwave radiative budgets, were calculated by considering the uncertainties for all the calculation inputs combined. Note here that when more than one variable is considered with uncertainty, all possible combinations are considered and can offset each other.

3. Results

3.1. *Albedo estimations*

Surface albedo varied from around 0.10 to 0.26 when considering all sites (see Fig. 2), which represent usual values reported in the literature for bare soil or vegetation covers (see Cescatti et al. (2012) for example). The lowest values were obtained over the saltmarsh scrubs ecosystem in *Tour du Valat (site 4).* They may be due to the presence of surface water in winter and to the specific type of vegetation which consisted for a large extent in succulent herbs appearing almost leafless (*Salicornia sp.*). Highest values were obtained over the agricultural *Avignon (site 1)* for wheat stubbles (see Davin et al. (2014)). Observed standard deviation values of surface albedo estimates over a 3×3-pixel area indicated that some of the sites are characterized by a significant spatial variability of biophysical parameters around the station. This was observed at the *Avignon (site 1)*. Such spatial variability may have an impact on the quality of the albedo retrievals since a Landsat pixel is around 1.5 to 4.5 larger than the footprint of the ground pyranometers.

[Insert Fig. 2 about here]

The evaluation of the albedo computed from each coefficient sets against ground data is presented in Table 4. $RMSE_A$ ranged from 0.025 to 0.033 (14 % to 19 % in terms of $RMSE_R$). In most cases, a significant negative bias, between -0.010 and -0.024 was obtained, in particular for estimations using middle infrared bands: *m2*, *m3, m8* and *m10*. After subtracting the bias, performances of most of the coefficient sets improved. Similar performances were obtained for coefficient sets which did not include middle infrared bands ($RMSE_A$ between 0.024 to 0.028). Improvement of performances was larger for the coefficient sets including middle infrared bands (*m2*, *m3, m8* and *m10)* leading to the lowest $RMSE_A$ (0.022 to 0.024). After unbiasing, the performances of each coefficient sets were in the range of albedo estimates over independent experimental data sets (*e.g.*, Liang et al. (2002); Liang et al. (2005); Tasumi et al. (2008); Franch et al. (2014)).

[Insert Table 4 about here]

Possible sources of bias in albedo estimates were: the calibration of field sensors, the calibration and the correction of radiometric signals from ETM+ and the differences in spectral bands between ETM+ and the other sensors. Other possible sources of bias were related to the way the anisotropy of surface reflectance is accounted in albedo calculations

(Franch et al. 2014) and/or on atmospheric corrections. Our calculations of albedo from Landsat reflectances acquired at nadir were not explicitly accounting for surface reflectance anisotropy. However, the NTB procedures were originally calibrated over measured apparent albedo or simulated hemispherical albedo implying that the weighting coefficients in Eq. (2) account, at least partially, for anisotropy impact (Jacob and Olioso 2002). The atmospheric corrections scheme used in the elaboration of TOC spectral reflectance product by MUSCATE considered a constant amount of precipitable water, while it can significantly change over space and time and have a significant impact on near infrared and middle infrared wavebands (Vermote et al. (1997); Bryant et al. (2003)). A previous evaluation of the correction method (Hagolle et al. (2008) for the Formosat-2 sensor), presented small underestimations of spectral reflectances (see Fig. 11 from Hagolle et al. (2008)).

3.2. *Emissivity estimations*

No previous study proposed a calibrated emissivity model directly applicable over our study area. Thus, emissivity measurements at our sites, or over similar targets, were used to analyze the variability of the input parameters required by Eq. (10) to relate emissivity to *NDVI* (ε_s, ε_∞ , $NDVI_s$, $NDVI_s$, k). Parameter values are given in Fig. 3.

[Insert Fig. 3 about here]

The range of spectral emissivities $\varepsilon_{\lambda_1-\lambda_2}$ computed from spectral reflectances of soil samples (Lesaignoux et al. 2013) showed a low variability from one sample to another and a dependence on soil moisture (Table 3, Fig. 3): from 0.963 to 0.986 in the 10.4–12.5 μm band and from 0.956 to 0.981 in the 8.0–13.5 μm band. These values agreed with emissivities of bare soils measured in the field in the same area by Labed and Stoll (1991), Coll et al. (2001) and Coll et al. (2002) (Table 2, Fig. 3). Variations related to changes in soil moisture were also in agreement with Mira et al. (2007) and Mira et al. (2010). For full vegetation canopies, Table 2 provides emissivity ranging from 0.980 to 0.983 in the Landsat waveband and between 0.980 and 0.995 in the 8.0–13.5 µm band (however, very few data were available in the Landsat spectral range). Variations of soil sample *NDVI* between 0.08 and 0.32 (Table 3) were in agreement with *NDVI* values derived from soil pixels extracted from Landsat images.

In order to account for the variability of emissivity and *NDVI,* we defined three sets of parameters resulting in three *NDVI* – emissivity curves in each spectral range (Fig. 3). *Curve B* provided an intermediate estimation of emissivities that was considered as a nominal emissivity model for our area. *Curve A* and *Curve C* provided lower and higher values of emissivity. These two other models were considered to define an uncertainty in emissivity estimation. The effect of uncertainty in spectral reflectances into the emissivity estimation (through relationship with NDVI) was not analyzed here given its small impact (<0.001).

3.3. *Estimation of surface temperature*

Land surface temperature estimated from TOC brightness temperature products were compared to ground based measurements over all measurement sites and dates (Fig. 4, Table 5). $RMSE_A$ was in the order of 1.7 K for emissivity *Curve B* ($\varepsilon_{10.4\text{-}12.5\ \mu m}$), mostly due to larger scatter at high temperatures for *Tour du Valat* and *Avignon sites*. $RMSE_A$ for *Curve A* and *Curve C* were in the same order. The different emissivity curves generated changes in bias from -0.1 K for the highest emissivity (*Curve C*) to +0.6 K for the lowest emissivity (*Curve A*). The best performances were obtained over homogeneous grassland

(*Domaine du Merle* and *Coussouls sites*). Performances were reduced over more heterogeneous sites: at *Tour du Valat* the surface was composed by patches of bare soil and vegetation, and the *Avignon site* represented a small crop field (2 ha) with in-field variability and surrounded by various other surfaces. If data from *Avignon (site 1)* were not considered, the $RMSE_A$ improved by 0.2 K (Fig. 4). Another source of errors may be related to the land surface emissivity of the sansouire ecosystem in *Tour du Valat (site 4)*. Actually no information existed on emissivity of such type of ecosystem with a high salt level and a large amount of leafless plants. As *NDVI* values were low due to the specific vegetation (see also the low albedo values), the emissivity could have been significantly underestimated using Eq. (10) leading to a significant overestimation of surface temperature, in particular at high temperature (Olioso 1995a; Olioso et al. 2013). However, the results were reasonable and consistent with the accuracy found in other studies (Li et al. (2004); Jiménez-Muñoz et al. (2009); Coll et al. (2010)).

[Insert Fig. 4 about here]

[Insert Table 5 about here]

3.4. *Estimation of net radiation*

Net radiation estimated from Landsat-7 data shows typical variations in time and space as a function of incident radiation and surface conditions (Fig. 5 and Fig. 6). Overall, surface net radiation varies from around 130 Wm^{-2} for a high albedo area in winter (200 Wm^{-2} in average over the whole image) to 790 Wm^{-2} for a dark and wet area in summer (600 Wm^{-2} in average). For a given day, spatial variations in *Rn* were in a range close to 50 % of its areal average depending on albedo and surface temperature level in relation to surface characteristics and land use (range from ~100 Wm^{-2} in winter to ~300 Wm^{-2} in summer). Evaluation of net radiation estimates showed a good agreement for all type of surfaces in general with a limited bias (Table 6 and Fig. 7). $RMSE_A$ were around 20 Wm^{-2} whatever the albedo model used. When using unbiased albedo models, $RMSE_A$ changed only slightly. Relative *RMSE* were in the order of 5 %, which showed that the sensitivity of net radiation to errors in albedo estimation was low (error in albedo were up to almost 20 %). In a similar way, standard deviations of net radiation estimates given in Fig. 7 were low indicating a low spatial variability in comparison to albedo (except for a pair of data from *Avignon (site 1)*).

[Insert Fig. 5 about here]

[Insert Fig. 6 about here]

[Insert Table 6 about here]

[Insert Fig. 7 about here]

3.5. *Uncertainty analysis*

Uncertainties in net radiation estimation presented strong seasonal patterns in correlation with the seasonal cycle of incident radiations, in particular solar irradiance, and net radiation (Fig. 8 and Table 7). They also presented strong spatial variability in relation to the variation of surface variables related to land use (Fig. 9). The North East – South West gradient observed in Fig. 9 resulted from the spatial variation of incoming radiation.

[Insert Fig. 8 about here]

[Insert Table 7 about here]

[Insert Fig. 9 about here]

Net radiation uncertainties were first analyzed in Table 7 as a function of uncertainties in input quantities for a typical winter day and a typical summer day (which usually presented the lowest and highest uncertainty levels, respectively). The uncertainty in net radiation was strongly dependent on the uncertainties in incoming radiation measurements and less dependent on the uncertainties in albedo and land surface temperature retrievals.

Net radiation uncertainties coming from uncertainties in land surface emissivities ($\delta\varepsilon_{8.0\text{-}13.5\ \mu m}$<0.010 or $\delta\varepsilon_{10.4\text{-}12.5\ \mu m}$<0.011) or from incoming atmospheric radiation in the measurement spectral band ($\delta R_{LW}{}^{\downarrow}{}_{10.4\text{-}12.5\mu m}$<7.3 Wm^{-2}) were negligible, and besides, their contributions compensated each other when considered their combination ($\delta Rn(\varepsilon_{8.0\text{-}13.5\ \mu m},\ \varepsilon_{10.4\text{-}12.5\ \mu m},\ R_{LW}{}^{\downarrow}{}_{10.4\text{-}12.5\mu m})$~0 Wm^{-2}). In the following, we detailed only the results for the most influencing factors (incident radiations, estimated albedo and remote sensing products of reflectances and brightness temperature).

3.5.1. *Global uncertainties in net radiation*

Global uncertainty in net radiation (δRn) estimation ranged between 40 Wm^{-2} in winter and 100 Wm^{-2} in summer (Fig. 8a), representing around 15 and 20 % of the net radiation, respectively. NB: these uncertainties were calculated by accounting only for albedo models designed for Landsat (see below). Overall, δRn was equally distributed between the shortwave and longwave radiative budgets (Fig. 8b–c). In summer, the uncertainty in the solar absorption was slightly dominant. In winter, the uncertainty in net longwave radiation was slightly dominant. Spatial variations were larger in summer and almost fully related to uncertainties in solar absorption estimation (Fig. 9a-c).

3.5.2. *Uncertainties in incoming radiation*

The input variables influencing the most the uncertainty in net radiation were the uncertainties in *in situ* measurements of incoming shortwave and longwave radiations (Fig. 8d–e). $R_{SW}^{\downarrow}$ uncertainties of 5 % were associated with *Rn* uncertainties varying from 10 to 40 Wm^{-2}. $R_{LW}^{\downarrow}$ uncertainties of 8 % were associated with *Rn* uncertainties varying from 20 to 30 Wm^{-2}. Together these represented around 70 % of the global uncertainties in net radiation and varied with the season.

3.5.3. *Uncertainties in albedo and spectral reflectances*

Uncertainty in estimated albedo was stable along the experimental period of time. When considering all the albedo models together uncertainty was up to 0.023 (0.017 as a median), which resulted in uncertainties in net radiation from 5 to 50 Wm^{-2} (Fig. 8f). However, the largest uncertainty levels were obtained over few specific areas corresponding mostly to quarries and industrial areas for which albedo models were not appropriate (industrial buildings, oil refinery, oil storage tanks areas, large asphalt zones, salt storage areas…) (Fig. 9d). Unbiased albedo models reduced uncertainties by almost 50 %. Further, when only unbiased albedo models originally defined for Landsat sensors were considered, uncertainties were considerably reduced: $\delta\alpha$ between 0.002 and 0.005 (0.003 as a median) and $\delta Rn(\alpha)$ below 10 Wm^{-2} (around 2 Wm^{-2} as a median) (Fig. 8g). Fig. 9e showed that the largest uncertainties were still obtained over industrial areas, but also over irrigated fields (paddy rice and irrigated grassland) and some wetlands. This might be related to the sensitivity of MIR reflectances to background reflectance from soil or water under vegetation.

Uncertainties in spectral reflectances $\delta\rho_i$ (5 % for all bands) resulted in $\delta Rn(\rho_i)$ almost twice larger than $\delta Rn(\alpha)$ when considering only unbiased albedo models designed for Landsat (in a similar order as when considering all the unbiased albedo model together). Spatial variations were related to the level of reflectance and the lowest uncertainties were obtained over wetlands and forested areas (Fig. 9f). Given values from Table 7, the reader could calculate the $\delta Rn(\rho_i)$ derived from other $\delta\rho_i$ values, as it varies proportionally.

Overall, the combination of albedo model and reflectance uncertainties ended up in an uncertainty between few Wm^{-2} and 25 Wm^{-2} (median values between 4 and 13 Wm^{-2}) in calculation of Rn.

3.5.4. *Uncertainties in the emission term*

The uncertainties in the emission term depended on the uncertainties in TOC brightness temperature $\delta Tb_{10.4\text{-}12.5\mu m}$, in emissivities $\delta\varepsilon_{10.4\text{-}12.5\mu m}$ and $\delta\varepsilon_{8.0\text{-}13.5\mu m}$, and in incident radiation $\delta R_{LW}{}^{\downarrow}{}_{10.4\text{-}12.5\mu m}$. $\delta Tb_{10.4\text{-}12.5\mu m}$ (set to 1.0 K) was the main driver, generating $\delta Rn(Tb_{10.4\text{-}12.5\mu m})$ between 5 and 7 Wm^{-2} all year long with almost no variations. The second driver was $\delta\varepsilon_{10.4\text{-}12.5\mu m}$. The other factors were negligible. Given values from Table 7, the reader could calculate the $\delta Rn(Tb_{10.4\text{-}12.5\mu m})$ derived from other $\delta Tb_{10.4\text{-}12.5\mu m}$, as it varies proportionally.

Overall, uncertainty in the emission term was almost constant around 8 Wm^{-2} which represented 30 % of the global uncertainty in the net thermal radiation uncertainty. Fig. 9g shows that this uncertainty was also spatially homogeneous.

4. Discussion

In this study we evaluated surface net radiation, albedo and surface temperature estimates derived from Landsat-7 over various surface types. These evaluations were performed both in terms of errors by comparison to *in situ* measurements and in terms of uncertainties in relation to uncertainties in the variables required for the computation of *Rn*. Concerning evaluation of remote estimates against *in situ* data, windows of 3×3 pixels were arbitrarily considered to take into account possible geolocation errors and include the measurement footprint of the sensors, characterized by their Point Spread Function (which implies in particular that the contribution to the signal for each pixel originates from a larger surface than the pixel size, Mira et al. (2015)). We expect that the variability of the 3×3 window is an indication of the variability of the area and that it can be an indication of the confidence in the comparison. However, there was no fully adequate way for matching information since the two types of measurements (satellite and *in situ*) had different footprint shapes and no higher resolution information was available for analyzing the spatial variability within each footprint.

In our estimations, net radiation varied from a minimum value of 130 Wm^{-2} to a maximum of 790 Wm^{-2} depending on the seasons, surface types and land use. A good agreement with *in situ* measurements of net radiation was found for all surface types ($RMSE_A$~20 Wm^{-2}). However, the computation of net radiation from both Landsat images and *in situ* measurements used the same measurements of incident radiations ($R_{SW}^{\downarrow}$ and $R_{LW}^{\downarrow}$). Thus, considering the uncertainties in incident radiations, the evaluation of estimated *Rn* was clearly optimistic. This explained that net radiation evaluations in Fig. 7 always laid well inside of the level of net radiation uncertainties (45 Wm^{-2} to 85 Wm^{-2} from winter to summer). This was not the case for albedo (Fig. 2) and surface temperature (Fig. 4).

Estimations of albedo from Landsat data were obtained by applying the NTB conversion method using different coefficient sets. Albedo were within a large range of values (~0 to ~0.6) indicating a large spatial variability depending on land use. When evaluated against ground data, the albedo obtained with any of the coefficient sets used in the NTB conversion, except one, were showing a significant negative bias. This bias was higher than uncertainties related to the calibration of the remote sensor (evaluated to 5 % in spectral reflectances (Chander et al. 2009)). Underestimation of albedo estimated from Landsat data were also recently reported by Shuai et al. (2011), Roman et al. (2013), and Franch et al. (2014). The latter demonstrated that it was possible to reduce the bias by improving both *1)* the way anisotropy of surface reflectance is accounted in the albedo calculation and *2)* the atmospheric corrections by introducing local measurements of atmospheric parameters (from the AERONET network). This raises the question of the evaluation of the accuracy of operational spectral reflectance products (or pre-operational products as those used in our study). These products are usually based on more systematic estimation of atmospheric parameters which are less accurate. This also militates in favor of the development of detailed albedo products based on the merging of Landsat nadir reflectance and BRDF information from other sensors such as MODIS or PROBA-V. After unbiasing, albedo estimates were within the range of performances observed over independent experimental data sets ($RMSE_A$ ~0.022–0.024), and as expected the best results were obtained for albedo coefficient sets that were derived for Landsat sensors. This indicated the necessity of accounting for the spectral characteristics of the sensors in the derivation of albedo models. It is interesting to notice that while the different coefficient sets were derived for Landsat sensors using different methods, the estimated albedo remained in a narrow range as shown by the low uncertainty related to the choice of coefficient sets (Fig. 8g): calibration against surface reflectance models (Liang 2000), against ground measurements (Dubayah (1992); Duguay and Ledrew (1992); Bsaibes et al. (2009)) or on the basis of theoretical spectral distribution (Tasumi et al. 2008). Nevertheless, if we have to retain one single set of coefficients for computing albedo from Landsat data, model m_3 proposed by Duguay and Ledrew (1992) would be a good option (considering our results it would have to be unbiased). This coefficient set is the only one among the sets we have tested that does not include the blue band *b1* which is usually highly sensitive to atmospheric corrections and can generate noisy reflectance data.

Results from the evaluation of surface temperature against ground measurements showed $RMSE_A$ of 1.7 K. This was in the range of the uncertainties we evaluated for the derivation of surface temperature as a function of brightness temperature and surface emissivity (~1.5 K in Table 7). The uncertainty in surface temperature may increase if either the available information for deriving brightness temperature product is limited (*e.g.*, atmospheric profiles in temperature and moisture) or land surface emissivity is not well known. This may be enhanced in specific situations where the derivation of brightness temperature and surface temperature are more sensitive to input information, as for a high level of moisture in the atmosphere or for a large variability of land surface emissivity (in particular for area with the presence of sandy soils). Frequent errors in satellite-based land surface temperature of vegetated surfaces due to incomplete emissivity and atmospheric corrections were reported up to 2 to 5 K for various sensors (Li et al. (2004); Sobrino et al. (2004); Wang and Liang (2009a); Guillevic et al. (2012); Hulley et al. (2012); Guillevic et al. (2014)).

Uncertainties in the derivation of albedo and surface temperature had limited impacts on the uncertainty in net radiation estimation. Albedo, together with spectral reflectances represented only 10 % (winter) to 15 % (summer) of the global uncertainty in net radiation and the emission term 20 % (winter) to 10 % (summer). The largest uncertainties were related to the estimation of incident radiations: more than two thirds of the uncertainty in net radiation estimation. When estimating net radiation from remote sensing data, spatial measurements or estimation of incident radiation are required to *1)* describe the spatial variability (which is often not large in cloudless conditions at the scale of a Landsat image) and *2)* to evaluate incident radiations in areas without adequate ground meteorological network. Several methods were proposed to estimate incident radiation from remote sensing (see a review by Liang et al., 2010). They usually provide irradiance data with uncertainties around twice larger than ground measurements. In general, estimation of solar irradiance is less accurate than estimation of downwelling longwave radiation: around 50 Wm^{-2} to 100 Wm^{-2} for $R_{SW}{\downarrow}$ and 15 Wm^{-2} to 40 Wm^{-2} for $R_{LW}{\downarrow}$ (Wang and Liang (2009b); Liang et al. (2010); Bisht and Bras (2011); Lefèvre et al. (2013); Garrigues et al. (2015)). In our analysis, the use of remote sensing products of incident radiations, in particular solar irradiance, would significantly increase the uncertainty level of the retrieved net radiation, possibly up to 130 Wm^{-2}. However, reported evaluation of net radiation estimations are usually well inside this uncertainty level. Possible improvements for the estimation of solar irradiance, by up to 40 %, were recently shown by including better descriptions of aerosol and water vapor contents (Lefèvre et al. (2013); Ceamanos et al. (2014)). However, these methodologies are not yet used to derive operational products.

Overall, we could generalize the results from this study to other study areas and sensors. Nevertheless, special attention should be paid to the characterization of emissivity as it requires a good knowledge of the spectral characteristics of all soils and canopy covers of the ecosystem unusually available. In our experiment, emissivities had a low impact, but uncertainties in emissivity estimation were low. In other areas, when emissivity of dry bare soil can be significantly lower (*e.g.*, Van de Griend and Owe (1993)) or when soils with very different emissivities coexist over the same area, it would be possible that impact on uncertainties in net radiation increases. However, this impact would be still lower than the impact of incident radiation uncertainties.

Our study was only considering net radiation and further efforts have to be done for analyzing uncertainties in heat flux estimation and in particular evapotranspiration. The impact of the uncertainties in the estimation of surface temperature will have to be assessed in more details as surface temperature is crucial information for partitioning heat fluxes into its latent and sensible components. Simple calculations show that uncertainties of 1 K and 3 K in surface temperature may generate uncertainties around 15 % and 40 % in evapotranspiration estimation. We should also notice that large uncertainty levels observed from uncertainties in spectral reflectances and albedo were located over few specific regions typically corresponding to quarries and industrial areas. From a point of view of directly estimating surface energy fluxes, we could consider that such areas were not of special interest for our study, downplaying them. However, a more thorough study is required to analyze whether those pixels are relevant or not to correctly estimate evapotranspiration following approaches like SEBAL (Bastiaanssen et al. 1998), the triangle method (Jiang and Islam 1999) or the Simplified Surface Energy Balance Index model (S-SEBI, Roerink et al. (2000)). These approaches consider the spatial variability of reflectance or albedo for defining wet and dry areas which are used to bound evapotranspiration evaluation to minimum and maximum levels.

5. Conclusion

The level of uncertainties reported in this study for net radiation is usually larger than errors reported in other studies. For example, Kustas and Norman (1996) reviewed various methods of estimating the net shortwave and longwave radiation fluxes and found that a variety of remote sensing methods of surface net radiation estimation had an uncertainty of 5–10 % compared with ground-based observations on meteorologically temporal scales. In our case, uncertainties were in the 15–20 % range. Actually, previous assessment of net radiation estimates from remote sensing data were usually based on the comparison to ground data only, without considering a formal analysis of uncertainties and their sources.

In our study, a simple definition of uncertainty was used in order to provide an evaluation of the possible errors in the estimation of net radiation (and intermediate variables). Error analysis based on *RMSE* calculations also considers an averaged impact over datasets which have usually a limited number of individual data. The analysis we performed in our study provides more generic information as uncertainties are mostly independent of the data used for computing *RMSE*.

We believe that the uncertainty evaluations presented in this study can be easily transferred to the analysis of mapping net radiation from other space or airborne sensors. In any cases, the uncertainties related to the estimation of incident radiations will be the main source of uncertainties in the estimation of net radiation. This has to be considered deeper in future analysis of energy flux mapping. Up to now, a large amount of efforts in the flux mapping community have been focused both on the estimation of intermediate land surface variables (albedo, emissivity, surface temperature) and on the derivation of flux calculation algorithms. Our study shows that improvements in algorithms to estimate albedo, surface emissivity and surface temperature from remote sensing would reduce net radiation uncertainties only marginally. We believe that in most situations, standard land products such as those generated by the THEIA Land Data Centre, are accurate enough to provide net radiation estimation from Landsat data. At present, TOC spectral reflectances are provided. In the next future, new products will be available including surface temperature and albedo.

We are currently developing the EVASPA tool (Evapotranspiration Assessment from SPAce, Gallego-Elvira et al. (2013)) for analyzing the impact of the uncertainties in net radiation and intermediate variables estimation on the estimation of evapotranspiration from remote sensing data. This tool makes also possible to analyze uncertainties in net radiation and evapotranspiration considering different time scale: instantaneous (as in the present study), daily, monthly and yearly.

Acknowledgements

This work was made through different projects funded by the National Centre for Space Studies, CNES (TOSCA) and the European SIRRIMED (Sustainable use of irrigation water in the Mediterranean) FP7 project (www.sirrimed.org). Mira was endorsed by a postdoctoral contract within the VALi+d program from Generalitat Valenciana (Spain), followed by a CNES postdoctoral contract and a “Juan de la Cierva” postdoctoral contract from the Spanish Ministry of Economy and Competitiveness. Gallego-Elvira was endorsed by a postdoctoral fellowship from the Ramon Areces Foundation.

References

Abrams, M.J., & Hook, S.J. (2013). NASA's Hyperspectral Infrared Imager (HyspIRI). *Thermal Infrared Remote Sensing, Remote Sensing and Digital Image Processing. Kuenzer, C. and Dech, S., Springer Netherlands, 17*, 117-130, DOI 110.1007/1978-1094-1007-6639-1006_1006

Anderson, M.C., Allen, R.G., Morse, A., & Kustas, W.P. (2012). Use of Landsat thermal imagery in monitoring evapotranspiration and managing water resources. *Remote Sensing of Environment, 122*, 50-65

Anton, Y.A., & Ross, Y.K. (1990). Emissivity of a soil vegetation system. *Soviet Journal of Remote Sensing, 7*, 859-869

Baillarin, S., Gigord, P., & Hagolle, O. (2008). Automatic registration of optical images, a stake for future missions: Application to ortho-rectification, time series and mosaic products. In, *IEEE International Geoscience and Remote Sensing Symposium Proceedings* (pp. 1112-1115). Boston, MA, USA

Bastiaanssen, W.G.M., Menenti, M., Feddes, R.A., & Holtslag, A.A.M. (1998). A remote sensing surface energy balance algorithm for land (SEBAL) - 1. Formulation. *Journal of Hydrology, 213*, 198-212

Berk, A., Anderson, G.P., Acharya, P.K., Hoke, M.L., Chetwynd, J.H., Bernstein, L.S., Shettle, E.P., Matthey, M.W., & Adler-Golden, S.M. (2003). MODTRAN4 Version 3 Revision 1 Users Manual. In, *AFRL Thechnical Report*. Hanscom AFB, USA

Bhattacharya, B.K., Mallick, K., Patel, N.K., & Parihar, J.S. (2010). Regional clear sky evapotranspiration over agricultural land using remote sensing data from Indian geostationary meteorological satellite. *Journal of Hydrology, 387*, 65-80

Bisht, G., & Bras, R.L. (2011). Estimation of Net Radiation From the Moderate Resolution Imaging Spectroradiometer Over the Continental United States. *Ieee Transactions on Geoscience and Remote Sensing, 49*, 2448-2462

Brest, C.L., & Goward, S.N. (1987). Deriving surface albedo measurements form narrow-band satellite data. *International Journal of Remote Sensing, 8(3)*, 351-367

Bryant, R., Moran, M.S., McElroy, S.A., Holifield, C., Thome, K.J., Miura, T., & Biggar, S.F. (2003). Data continuity of Earth Observing 1 (EO-1) Advanced Land Imager (ALI) and Landsat TM and ETM+. *Ieee Transactions on Geoscience and Remote Sensing, 41*, 1204-1214

Bsaibes, A., Courault, D., Baret, F., Weiss, M., Olioso, A., Jacob, F., Hagolle, O., Marloie, O., Bertrand, N., Desfond, V., & Kzemipour, F. (2009). Albedo and LAI estimates from FORMOSAT-2 data for crop monitoring. *Remote Sensing of Environment, 113*, 716-729

Caselles, E., Valor, E., Abad, F., & Caselles, V. (2012). Automatic classification-based generation of thermal infrared land surface emissivity maps using AATSR data over Europe. *Remote Sensing of Environment, 124*, 321-333

Ceamanos, X., Carrer, D., & Roujean, J.L. (2014). Improved retrieval of direct and diffuse downwelling surface shortwave flux in cloudless atmosphere using dynamic estimates of aerosol content and type: application to the LSA-SAF project. *Atmospheric Chemistry and Physics, 14*, 8209-8232

Cescatti, A., Marcolla, B., Vannan, S.K.S., Pan, J.Y., Roman, M.O., Yang, X.Y., Ciais, P., Cook, R.B., Law, B.E., Matteucci, G., Migliavacca, M., Moors, E., Richardson, A.D., Seufert, G., & Schaaf, C.B. (2012). Intercomparison of MODIS albedo retrievals and in situ measurements across the global FLUXNET network. *Remote Sensing of Environment, 121*, 323-334

Chander, G., Markham, B.L., & Helder, D.L. (2009). Summary of current radiometric calibration coefficients for Landsat MSS, TM, ETM+, and EO-1 ALI sensors. *Remote Sensing of Environment, 113*, 893-903

Ciais, P., Reichstein, M., Viovy, N., Granier, A., Ogée, J., Allard, V., Aubinet, M., Buchmann, N., Bernhofer, C., & Carrara, A. (2005). Europe-wide reduction in primary productivity caused by the heat and drought in 2003. *Nature, 437*, 529-533

Cheng, J., Liang, S., Yao, Y., & Zhang, X. (2013). Estimating the optimal broadband emissivity spectral range for calculating surface longwave net radiation. *Ieee Geoscience and Remote Sensing Letters, 10(2)*, 401-405

Coll, C., Caselles, V., Rubio, E., Sospedra, F., & Valor, E. (2001). Analysis of thermal infrared data from the Digital Airborne Imaging Spectrometer. *International Journal of Remote Sensing, 22(18)*, 3703-3718

Coll, C., Caselles, V., Rubio, E., Valor, E., Sospedra, F., Baret, F., Prevot, L., & Jacob, F. (2002). Temperature and emissivity extracted from airborne multi-channel data in the ReSeDA experiment. *Agronomie, 22*, 567-573

Coll, C., Valor, E., Caselles, V., & Niclòs, R. (2003). Adjusted Normalized Emissivity Method for surface temperature and emissivity retrieval from optical and thermal infrared remote sensing data. *Journal of Geophysical Research-Atmospheres, 108*

Coll, C., Galve, J.M., Sánchez, J.M., & Caselles, V. (2010). Validation of Landsat-7/ETM+ Thermal-Band Calibration and Atmospheric Correction With Ground-Based Measurements. *Ieee Transactions on Geoscience and Remote Sensing, 48*, 547-555

Crebassol, P., Lagouarde, J.P., & Hook, S. (2014). THIRSTY thermal infrared spatial system. In, *International Geoscience and Remote Sensing Symposium (IGARSS 2014)* (pp. 3021-3024). Québec, Canada

Crosetto, M., Ruiz, J.A.M., & Crippa, B. (2001). Uncertainty propagation in models driven by remotely sensed data. *Remote Sensing of Environment, 76*, 373-385

Davin, E.L., Seneviratne, S.I., Ciais, P., Olioso, A., & Wang, T. (2014). Preferential cooling of hot extremes from cropland albedo management. *Proceedings of the National Academy of Sciences of the United States of America, 111(27)*, 9757-9761

Dubayah, R. (1992). Estimating net solar-radiation using Landsat Thematic Mapper and digital elevation data. *Water Resources Research, 28*, 2469-2484

Duffour, C., Olioso, A., Demarty, J., Van der Tol, C., & Lagouarde, J.P. (2015). An evaluation of SCOPE: A tool to simulate the directional anisotropy of satellite-measured surface temperatures. *Remote Sensing of Environment, 158*, 362–375.

Duguay, C.R., & Ledrew, E.F. (1992). Estimating surface reflectance and albedo from Landsat-5 Thematic Mapper over rugged terrain. *Photogrammetric Engineering and Remote Sensing, 58(5)*, 551-558

Franch, B., Vermote, E.F., & Claverie, M. (2014). Intercomparison of Landsat albedo retrieval techniques and evaluation against in situ measurements across the US SURFRAD network. *Remote Sensing of Environment, 152*, 627-637

François, C., Ottle, C., & Prevot, L. (1997). Analytical parameterization of canopy directional emissivity and directional radiance in the thermal infrared. Application on the retrieval of soil and foliage temperatures using two directional measurements. *International Journal of Remote Sensing, 18*, 2587-2621

Gallego-Elvira, B., Olioso, A., Mira, M., Reyes-Castillo, S., Boulet, G., Marloie, O., Garrigues, S., Courault, D., Weiss, M., Chauvelon, P., & Boutron, O. (2013). EVASPA (EVapotranspiration Assessment from SPAce) tool: and overview. *Procedia Environmental Sciences, 19*, 303-310

Garcia-Santos, V., Valor, E., Caselles, V., Mira, M., Galve, J.M., & Coll, C. (2013). Evaluation of different methods to retrieve the hemispherical downwelling irradiance in the thermal infrared region for field measurements. *Ieee Transactions on Geoscience and Remote Sensing, 51*, 2155-2165

Garrigues, S., Olioso, A., Calvet, J.C., Martin, E., Lafont, S., Moulin, S., Chanzy, A., Marloie, O., Desfonds, V., Bertrand, N., & Renard, D. (2014). Evaluation of land surface model simulations of evapotranspiration over a 12 year crop succession: impact of the soil hydraulic properties. *Hydrol. Earth Syst. Sci. Discuss., 11*, 11687-11733

Garrigues, S., Olioso, A., Carrer, D., Decharme, B., Martin, E., Calvet, J.C., Moulin, S., & Marloie, O. (2015). Impact of climate, vegetation, soil and crop management variables on multi-year ISBA-A-gs simulations of evapotranspiration over a Mediterranean crop site. *Geosci. Model Dev. Discuss., 8*, 2053-2100

Gillespie, A., Rokugawa, S., Matsunaga, T., Cothern, J.S., Hook, S., & Kahle, A.B. (1998). A temperature and emissivity separation algorithm for Advanced Spaceborne Thermal Emission and Reflection Radiometer (ASTER) images. *Ieee Transactions on Geoscience and Remote Sensing, 36*, 1113-1126

Guillevic, P.C., Biard, J.C., Hulley, G.C., Privette, J.L., Hook, S.J., Olioso, A., Goettsche, F.M., Radocinski, R., Roman, M.O., Yu, Y., & Csiszar, I. (2014). Validation of Land Surface Temperature products derived from the Visible Infrared Imaging

Radiometer Suite (VIIRS) using ground-based and heritage satellite measurements. *Remote Sensing of Environment, 154*, 19-37

Guillevic, P.C., Privette, J.L., Coudert, B., Palecki, M.A., Demarty, J., Ottle, C., & Augustine, J.A. (2012). Land Surface Temperature product validation using NOAA's surface climate observation networks-Scaling methodology for the Visible Infrared Imager Radiometer Suite (VIIRS). *Remote Sensing of Environment, 124*, 282-298

Hagolle, O., Dedieu, G., Mougenot, B., Debaecker, V., Duchemin, B., & Meygret, A. (2008). Correction of aerosol effects on multi-temporal images acquired with constant viewing angles: Application to Formosat-2 images. *Remote Sensing of Environment, 112*, 1689-1701

Hagolle, O., Huc, M., Pascual, D.V., & Dedieu, G. (2010). A multi-temporal method for cloud detection, applied to FORMOSAT-2, VENμS, LANDSAT and SENTINEL-2 images. *Remote Sensing of Environment, 114(8)*, 1747-1755

Hagolle, O., Huc, M., Dedieu, G., & Petrucci, B. (2012). MACCS: a multisensor atmospheric correction and cloud screening processor. In, *ESA Sentinel-2 preparatory symposium 2012*. ESA-ESRIN, Frascaty, Italy, http://www.congrexprojects.com/docs/12c04_doc/3-sentinel2_symposium_hagolle.pdf (last access: November 2, 2015)

Hagolle, O., Huc, M., Villa Pascual, D., & Dedieu, G. (2015). A multi-temporal and multi-spectral method to estimate aerosol optical thickness over land, for the atmospheric correction of FormoSat-2, LandSat, VENμS and Sentinel-2 images. *Remote Sensing, 7*, 2668-2691

Harrison, T.R. (1960). Radiation pyrometry and its underlying principles of radiant heat transfer. In: John Wiley, New York, USA

Hulley, G.C., Hughes, C.G., & Hook, S.J. (2012). Quantifying uncertainties in land surface temperature and emissivity retrievals from ASTER and MODIS thermal infrared data. *Journal of Geophysical Research-Atmospheres, 117*

Idso, S.B. (1981). A set of equations for full spectrum and 8 μm to 14 μm and 10.5 μm to 12.5 μm thermal radiation from cloudless skies. *Water Resources Research, 17(2)*, 295-304

ISO (1992). Solar energy. Calibration of field pyranometers by comparison to a reference pyranometer. In, *International Organization for Standardization (ISO) 9847*

Jacob, F., Gu, X.F., Hanocq, J.F., Tallet, N., & Baret, F. (2003). Atmospheric corrections of single broadband channel and multidirectional airborne thermal infrared data: application to the ReSeDA experiment. *International Journal of Remote Sensing, 24*, 3269-3290

Jacob, F., & Olioso, A. (2002). Assessing recent algorithms devoted to albedo estimation using the airborne ReSeDa / PolDER database. In, *1st International Symposium on Recent Advances in Quantitative Remote Sensing* (pp. 191-198). Torrent, Valencia (Spain)

Jacob, F., Olioso, A., Gu, X.F., Su, Z.B., & Seguin, B. (2002a). Mapping surface fluxes using airborne visible, near infrared, thermal infrared remote sensing data and a spatialized surface energy balance model. *Agronomie, 22*, 669-680

Jacob, F., Olioso, A., Weiss, M., Baret, F., & Hautecoeur, O. (2002b). Mapping short-wave albedo of agricultural surfaces using airborne PolDER data. *Remote Sensing of Environment, 80*, 36-46

Jacob, F., Weiss, M., Olioso, A., & French, A. (2002c). Assessing the narrowband to broadband conversion to estimate visible, near infrared and shortwave apparent albedo from airborne PoIDER data. *Agronomie, 22*, 537

Jiang, L., & Islam, S. (1999). A methodology for estimation of surface evapotranspiration over large areas using remote sensing observations. *Geophysical Research Letters, 26*, 2773-2776

Jiménez-Muñoz, J.C., Cristóbal, J., Sobrino, J.A., Soria, G., Ninyerola, M., & Pons, X. (2009). Revision of the single-channel algorithm for land surface temperature retrieval from Landsat thermal-infrared data. *Ieee Transactions on Geoscience and Remote Sensing, 47*, 339-349

Kohsiek, W., Liebethal, C., Foken, T., Vogt, R., Oncley, S.P., Bernhofer, C., & Debruin, H.A.R. (2007). The energy balance experiment EBEX-2000. Part III: Behaviour and quality of the radiation measurements. *Boundary-Layer Meteorology, 123(1)*, 55-75

Kustas, W.P., & Norman, J.M. (1996). Use of remote sensing for evapotranspiration monitoring over land surfaces. *Hydrological Sciences Journal-Journal Des Sciences Hydrologiques, 41*, 495-516

L'Helguen, C., Donadieu, J., Leroy, M., Pacholczyk, P., Hagolle, O., Huc, M., Gasperi, J., Petrucci, B., Melet, O., Alves-Suana, F., Sarrazin, E., Lebegue, L., & Lonjou, V. (2014). MUSCATE: Multi-satellites, multi-sensors and multi-temporal THEIA data centre. In, *Proceedings of the 2014 conference on Big Data from Space (BiDS'14)* (pp. 113-116). ESA-ESRIN, Frascati, Rome (Italy)

Labed, J., & Stoll, M.P. (1991). Spatial variability of land surface emissivity in the thermal infrared band: Spectral signature and effective surface temperature. *Remote Sensing of Environment, 38*, 1-17

Lagouarde, J.-P., Bach, M., Sobrino, J.A., Boulet, G., Briottet, X., Cherchali, S., Coudert, B., Dadou, I., Dedieu, G., Gamet, P., Hagolle, O., Jacob, F., Nerry, F., Olioso, A., Ottle, C., Roujean, J.-l., & Fargant, G. (2013). The MISTIGRI thermal infrared project: scientific objectives and mission specifications. *International Journal of Remote Sensing, 34(9-10)*, 3437-3466

Lefèvre, M., Oumbe, A., Blanc, P., Espinar, B., Gschwind, B., Qu, Z., Wald, L., Schroedter-Homscheidt, M., Hoyer-Klick, C., Arola, A., Benedetti, A., Kaiser, J.W., & Morcrette, J.J. (2013). McClear: a new model estimating downwelling solar radiation at ground level in clear-sky conditions. *Atmospheric Measurement Techniques, 6*, 2403-2418

Leroy, M., Hagolle, O., Huc, M., Kadiri, M., Dedieu, G., Donadieu, J., Pacholczyk, P., L'Helguen, C., Petrucci, B., & Cherchali, S. (2014). MUSCATE : Operational Production Atmospheric Corrections and Monthly Composites Sentinel-2. In, *Sentinel-2 for science workshop*. Frascati, Rome (Italy), http://seom.esa.int/S2forScience2014/files/03_S2forScience-MethodsII_LEROY.pdf (last access: November 2, 2015)

Lesaignoux, A., Fabre, S., & Briottet, X. (2013). Influence of soil moisture content on spectral reflectance of bare soils in the 0.4-14 µm domain. *International Journal of Remote Sensing, 34(7)*, 2268-2285

Li, F.Q., Jackson, T.J., Kustas, W.P., Schmugge, T.J., French, A.N., Cosh, M.H., & Bindlish, R. (2004). Deriving land surface temperature from Landsat 5 and 7 during SMEX02/SMACEX. *Remote Sensing of Environment, 92*, 521-534

Liang, S., Shuey, C.J., Russ, A.L., Fang, H., Chen, M., Walthall, C.L., Daughtry, C.S.T., & Hunt Jr, R. (2002). Narrowband to broadband conversions of land surface albedo: II. Validation. *Remote Sensing of Environment, 84*, 25-41

Liang, S., Wang, K., Zhang, X., & Wild, M. (2010). Review on Estimation of Land Surface Radiation and Energy Budgets From Ground Measurement, Remote Sensing and Model Simulations. *Ieee Journal of Selected Topics in Applied Earth Observations and Remote Sensing, 3*, 225-240

Liang, S., Yu, Y., & Defelice, T.P. (2005). VIIRS narrowband to broadband land surface albedo conversion: formula and validation. *International Journal of Remote Sensing, 26(5)*, 1019-1025

Liang, S.L. (2000). Narrowband to broadband conversions of land surface albedo I Algorithms. *Remote Sensing of Environment, 76*, 213-238

Mattar, C., Franch, B., Sobrino, J.A., Corbari, C., Jiménez-Muñoz, J.C., Olivera-Guerra, L., Skokovic, D., Soria, G., Oltra-Carrio, R., Julien, Y., & Mancini, M. (2014). Impacts of the broadband albedo on actual evapotranspiration estimated by S-SEBI model over an agricultural area. *Remote Sensing of Environment, 147*, 23-42

Merlin, O., Chirouze, J., Olioso, A., Jarlan, L., Chehbouni, G., & Boulet, G. (2014). An image-based four-source surface energy balance model to estimate crop evapotranspiration from solar reflectance/thermal emission data (SEB-4S). *Agricultural and Forest Meteorology, 184*, 188-203

Mira, M., Olioso, A., Rivalland, V., Courault, D., Marloie, O., & Guillevic, P. (2014). Quantifying uncertainties in land surface temperature due to atmospheric correction: application to Landsat-7 data over a Mediterranean agricultural region. In, *International Geoscience and Remote Sensing Symposium (IGARSS)* (pp. 2375-2378). Quebec, Canada, USA

Mira, M., Valor, E., Boluda, R., Caselles, V., & Coll, C. (2007). Influence of soil water content on the thermal infrared emissivity of bare soils: Implication for land surface temperature determination. *Journal of Geophysical Research-Earth Surface, 112*

Mira, M., Valor, E., Caselles, V., Rubio, E., Coll, C., Galve, J.M., Niclòs, R., Sánchez, J.M., & Boluda, R. (2010). Soil Moisture Effect on Thermal Infrared (8-13-mu m) Emissivity. *Ieee Transactions on Geoscience and Remote Sensing, 48(5)*, 2251-2260

Mira, M., Weiss, M., Baret, F., Courault, D., Hagolle, O., Gallego-Elvira, B., & Olioso, A. (2015). The MODIS (collection V006) BRDF/albedo product MCD43D: Temporal course evaluated over agricultural landscape. *Remote Sensing of Environment*, *170*, 216-228

Norman, J.M., & Becker, F. (1995). Terminology in thermal infrared remote-sensing of natural surfaces. *Agricultural and Forest Meteorology, 77*, 153-166

Norman, J.M., Divakarla, M., & Goel, N.S. (1995). Algorithms for extracting information from remote thermal-IR observations of the Earth's Surface. *Remote Sensing of Environment, 51*, 157-168

Ogawa, K., & Schmugge, T.J. (2004). Mapping Surface Broadband Emissivity of the Sahara Desert Using ASTER and MODIS Data. *Earth Interactions, 8*, 1-14

Olioso, A. (1995a). Estimating the difference between brightness and surface temperatures for a vegetal canopy. *Agricultural and Forest Meteorology, 72(3-4)*, 237

Olioso, A. (1995b). Simulating the relationship between thermal emissivity and the normalized difference vegetation index. *International Journal of Remote Sensing, 16(16)*, 3211

Olioso, A., Chauki, H., Courault, D., & Wigneron, J.P. (1999). Estimation of evapotranspiration and photosynthesis by assimilation of remote sensing data into SVAT models. *Remote Sensing of Environment, 68,* 341-356

Olioso, A., Mira, M., Courault, D., Marloie, O., & Guillevic, P. (2013). Impact of surface emissivity and atmospheric conditions on surface temperatures estimated from top of canopy brightness temperatures derived from Landsat-7 data. In, *IEEE International Geoscience and Remote Sensing Symposium* (pp. 3033-3036). Melbourne, Australia

Olioso, A., Soria, G., Sobrino, J., & Duchemin, B. (2007). Evidence of low land surface thermal infrared emissivity in the presence of dry vegetation. *Ieee Geoscience and Remote Sensing Letters, 4*, 112-116

Pinty, B., & Verstraete, M.M. (1992). On the design and validation of surface bidirectional reflectance and albedo models. *Remote Sensing of Environment, 41*, 155-167

Ranson, K.J., Irons, J.R., & Daughtry, C.S.T. (1991). Surface albedo from bidirectional reflectance. *Remote Sensing of Environment, 35*, 201-211

Rivalland, V., Boulet, G., Mira, M., Brut, A., & Olioso, A. (2014). 6 years time-series of estimation and validation of land surface temperature from Landsat 5 & 7 archive on 3 plots of South-West of France. In, *4th International Symposium in Recent Advances in Quantitative Remote Sensing (RAQRSS'IV)*. Torrent, Valencia, Spain.

Roerink, G.J., Su, Z., & Menenti, M. (2000). S-SEBI: A simple remote sensing algorithm to estimate the surface energy balance. *Physics and Chemistry of the Earth Part B-Hydrology Oceans and Atmosphere, 25*, 147-157

Roman, M.O., Gatebe, C.K., Shuai, Y., Wang, Z., Gao, F., Masek, J.G., He, T., Liang, S., & Schaaf, C.B. (2013). Use of in situ and airborne multiangle data to assess MODIS and Landsat-based estimates of directional reflectance and albedo. *Ieee Transactions on Geoscience and Remote Sensing, 51*, 1393-1404

Rubio, E., Caselles, V., & Badenas, C. (1997). Emissivity measurements of several soils and vegetation types in the 8-14 μm wave band: Analysis of two field methods. *Remote Sensing of Environment, 59*, 490-521

Seguin, B., Becker, F., Phulpin, T., Gu, X.F., Guyot, G., Kerr, Y., King, C., Lagouarde, J.P., Ottle, C., Stoll, M.P., Tabbagh, A., & Vidal, A. (1999). IRSUTE: A minisatellite project for land surface heat flux estimation from field to regional scale. *Remote Sensing of Environment, 68*, 357-369

Sellers, P.J., Meeson, B.W., Hall, F.G., Asrar, G., Murphy, R.E., Schiffer, R.A., Bretherton, F.P., Dickinson, R.E., Ellingson, R.G., Field, C.B., Huemmrich, K.F., Justice, C.O., Melack, J.M., Roulet, N.T., Schimel, D.S., & Try, P.D. (1995). Remote-sensing of the land-surface for studies of global change - Models, algorithms, experiments. *Remote Sensing of Environment, 51*, 3-26

Shuai, Y., Masek, J.G., Gao, F., & Schaaf, C.B. (2011). An algorithm for the retrieval of 30-m snow-free albedo from Landsat surface reflectance and MODIS BRDF. *Remote Sensing of Environment, 115*, 2204-2216

Sobrino, J.A., Jiménez-Muñoz, J.C., & Paolini, L. (2004). Land surface temperature retrieval from LANDSAT TM 5. *Remote Sensing of Environment, 90*, 434-440

Sobrino, J.A., Raissouni, N., & Li, Z.L. (2001). A comparative study of land surface emissivity retrieval from NOAA data. *Remote Sensing of Environment, 75*, 256-266

Tang, R., Li, Z.-L., Jia, Y., Li, C., Sun, X., Kustas, W.P., & Anderson, M.C. (2011). An intercomparison of three remote sensing-based energy balance models using Large Aperture Scintillometer measurements over a wheat-corn production region. *Remote Sensing of Environment, 115*, 3187-3202

Tang, X., Li, H., Desai, A.R., Nagy, Z., Luo, J., Kolb, T.E., Olioso, A., Xu, X., Yao, L., & Kutsch, W. (2014). How is water-use efficiency of terrestrial ecosystems distributed and changing on Earth? *Scientific reports, 4*

Tasumi, M., Allen, R.G., & Trezza, R. (2008). At-surface reflectance and albedo from satellite for operational calculation of land surface energy balance. *Journal of Hydrologic Engineering, 13(2)*, 51-63

Valor, E., & Caselles, V. (1996). Mapping land surface emissivity from NDVI: Application to European, African, and South American areas. *Remote Sensing of Environment, 57*, 167-184

Van de Griend, A.A., & Owe, M. (1993). On the relationship between thermal emissivity and the normalized difference vegetation index for natural surfaces. *International Journal of Remote Sensing, 14*, 1119-1131

Van der Tol, C., Verhoef, W., Timmermans, J., Verhoef, A., & Su, Z. (2009). An integrated model of soil-canopy spectral radiances, photosynthesis, fluorescence, temperature and energy balance. *Biogeosciences, 6*, 3109–3129

Vermote, E.F., ElSaleous, N., Justice, C.O., Kaufman, Y.J., Privette, J.L., Remer, L., Roger, J.C., & Tanre, D. (1997). Atmospheric correction of visible to middle-infrared EOS-MODIS data over land surfaces: Background, operational algorithm and validation. *Journal of Geophysical Research-Atmospheres, 102*, 17131-17141

Wang, K., & Liang, S. (2009a). Evaluation of ASTER and MODIS land surface temperature and emissivity products using long-term surface longwave radiation observations at SURFRAD sites. *Remote Sensing of Environment, 113*, 1556-1565

Wang, W., & Liang, S. (2009b). Estimation of high-spatial resolution clear-sky longwave downward and net radiation over land surfaces from MODIS data. *Remote Sensing of Environment, 113*, 745-754

Wang, D., Liang, S., & He, T. (2014). Mapping high-resolution surface shortwave net radiation from Landsat data. *Ieee Geoscience and Remote Sensing Letters, 11*, 459-463

Weiss, M., Baret, F., Leroy, M., Begue, A., Hautecoeur, O., & Santer, R. (1999). Hemispherical reflectance and albedo estimates from the accumulation of across-track sun-synchronous satellite data. *Journal of Geophysical Research-Atmospheres, 104*, 22221-22232

Wittich, K.P. (1997). Some simple relationships between land-surface emissivity, greenness and the plant cover fraction for use in satellite remote sensing. *International Journal of Biometeorology, 41*, 58-64

WMO (2008). Guide to meteorological instruments and methods of observation, Chapter 7: Measurement of radiation. In, *World Meteorological Organization (WMO)-No.8*. Geneve, Switzerland. ISBN 978-92-63-10008-5

WWW1 THEIA Land Data Centre. http://www.theia-land.fr/en (last access: November 2, 2015)

WWW2 The prototype MUSCATE production facility of THEIA Land Data Centre. http://www.cesbio.ups-tlse.fr/multitemp/?tag=muscate (last access: November 2, 2015)

WWW3 Radiosonde data from University of Wyoming. http://weather.uwyo.edu/upperair/sounding.html (last access: November 2, 2015)

WWW4 Kipp & Zonen, Instructions manual CNR1 net radiometer. Manual revision 5/11, 40 pp. [Available online at www.campbellsci.com/cnr1]. http://www.kippzonen.com/ (last access: November 2, 2015)

WWW5 The Eppley Laboratory, Inc. http://www.eppleylab.com/ (last access: November 2, 2015)

WWW6 Atmospheric Correction Parameter Calculator. http://atmcorr.gsfc.nasa.gov/

(last access: November 2, 2015)

Xia, J., Chen, J., Piao, S., Ciais, P., Luo, Y., & Wan, S. (2014). Terrestrial carbon cycle affected by non-uniform climate warming. *Nature Geoscience, 7*, 173-180

FIGURES

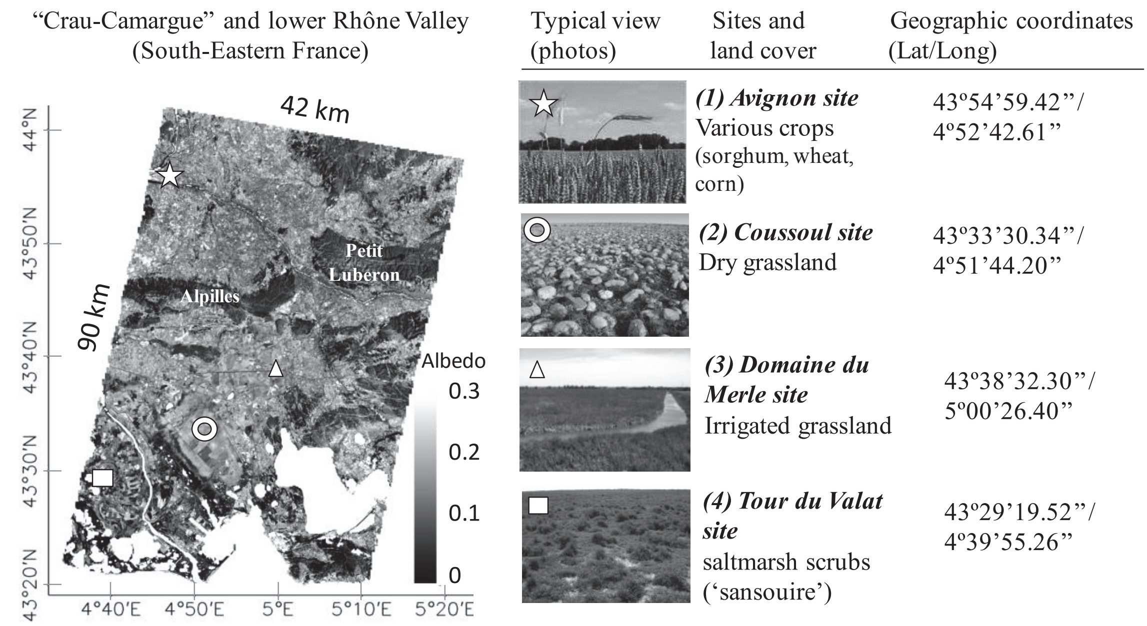

Fig. 1. Albedo map derived from the central workable part of the Landsat-7 ETM+ image acquired on July 8th, 2008 over the lower Rhône Valley, South-Eastern France. Typical view, main land cover and location of the instrumented sites used for this study.

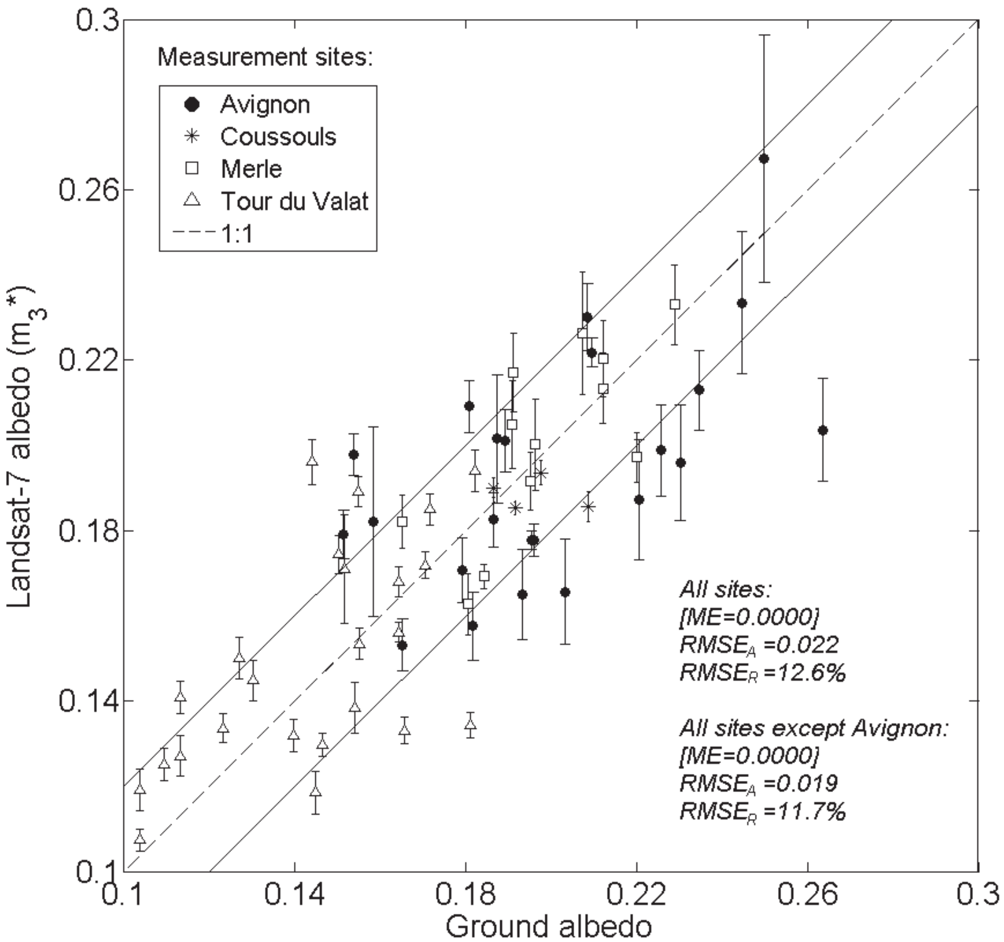

Fig. 2. Comparison of albedo estimates using Landsat-7 data (unbiased *m3* model) and *in situ* measurements over the sites. Error bars show the standard deviation of averaged data (*i.e.*, 3×3 pixels 30-m resolution) and solid lines denote an estimation for uncertainty in albedo. *ME*: bias; $RMSE_A$ and $RMSE_R$: absolute and relative Root Mean Square Error.

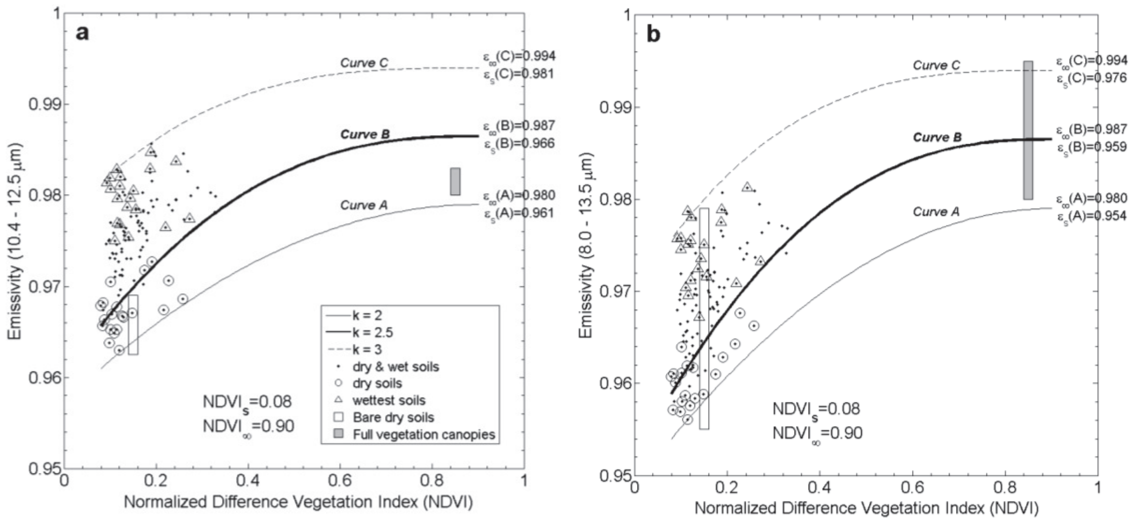

Fig. 3. Relationship between *NDVI* and emissivities for the 10.4–12.5 µm and the 8.0–13.5 µm spectral ranges following Wittich (1997)'s model (Eq. 10) and coefficient values given in Table 5. *Curve B* corresponds to the nominal values of emissivity considered in this study; *Curve A* and *Curve C* denote an estimation for uncertainty in emissivity; dots correspond to experimental data from Lesaignoux et al. (2013) over soils with different soil moisture content; white rectangle indicates the range of values corresponding to ground measurements over soil samples from Alpilles (Coll et al., 2001, 2002) and La Crau (Labed and Stoll, 1991); filled rectangle indicates the range of values corresponding to experimental measurements over surfaces with high *NDVI* (Coll et al., 2003, 2010; Olioso et al., 2007).

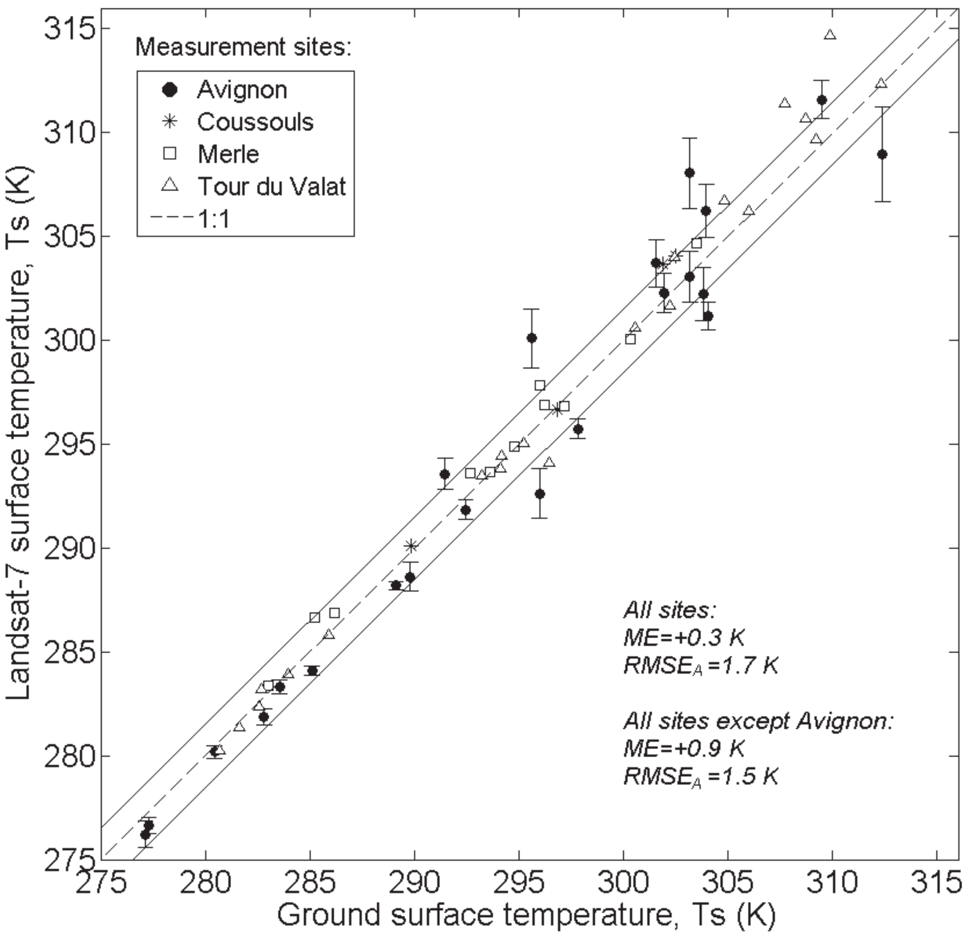

Fig. 4. Comparison of surface temperature estimates using Landsat-7 data and *in situ* measurements over the sites. Error bars (only significant for *Avignon site*) show the standard deviation of averaged data (*i.e.*, 3×3 pixels 60-m resolution) and solid lines denote an estimation for uncertainty in surface temperature. *ME*: bias; *RMSE$_A$*: absolute Root Mean Square Error.

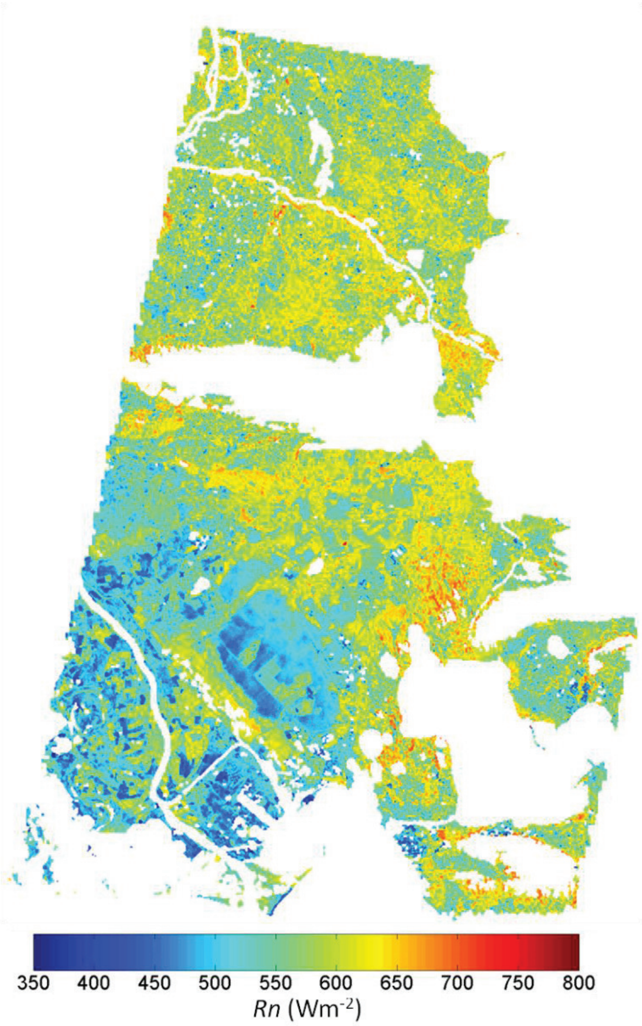

Fig. 5. Spatial distribution of net radiation estimates for the entire Landsat-7 image acquired at 10:30 UTC on July 8th, 2008 over the Crau-Camargue. It was used albedo model *m3* with no bias. Pixels with value higher than 800 or lower than 350 (a small percentage of the entire image) are masked in red and blue, respectively. Water, clouds, shadows, and pixels with an altitude higher than 100 m are masked in white.

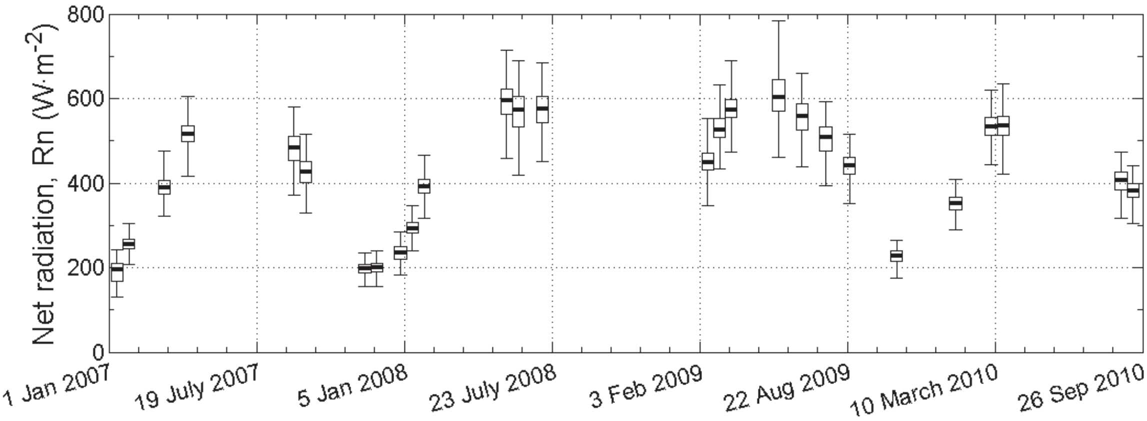

Fig. 6. Temporal variation of net radiation estimates using Landsat-7 data. It was used albedo model *m3* with no bias. Each boxplot belongs to an acquisition day and comprises the median (central thick line), the first and third quartile (inferior and superior edges of the boxes), and the extreme values excluding outliers (inferior and superior whiskers).

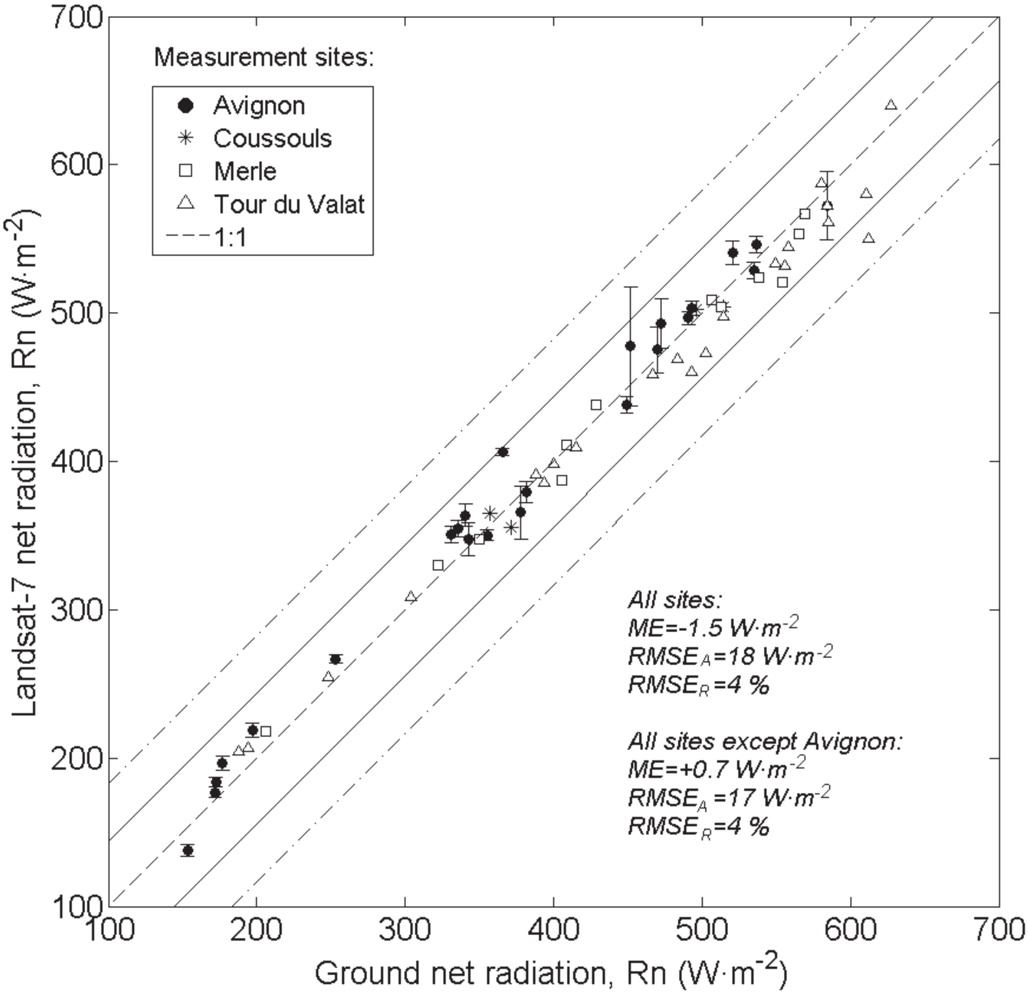

Fig. 7. Comparison of net radiation estimates using Landsat-7 data and *in situ* measurements over the sites. It was used albedo model *m3* with no bias. Error bars (only significant for *Avignon site*) show the standard deviation of averaged data (*i.e.*, 3×3 pixels 60-m resolution) and solid (respectively dash-dot) lines denote an estimation for minimum (respectively maximum) uncertainty in net radiation. *ME*: bias; $RMSE_A$ and $RMSE_R$: absolute and relative Root Mean Square Error.

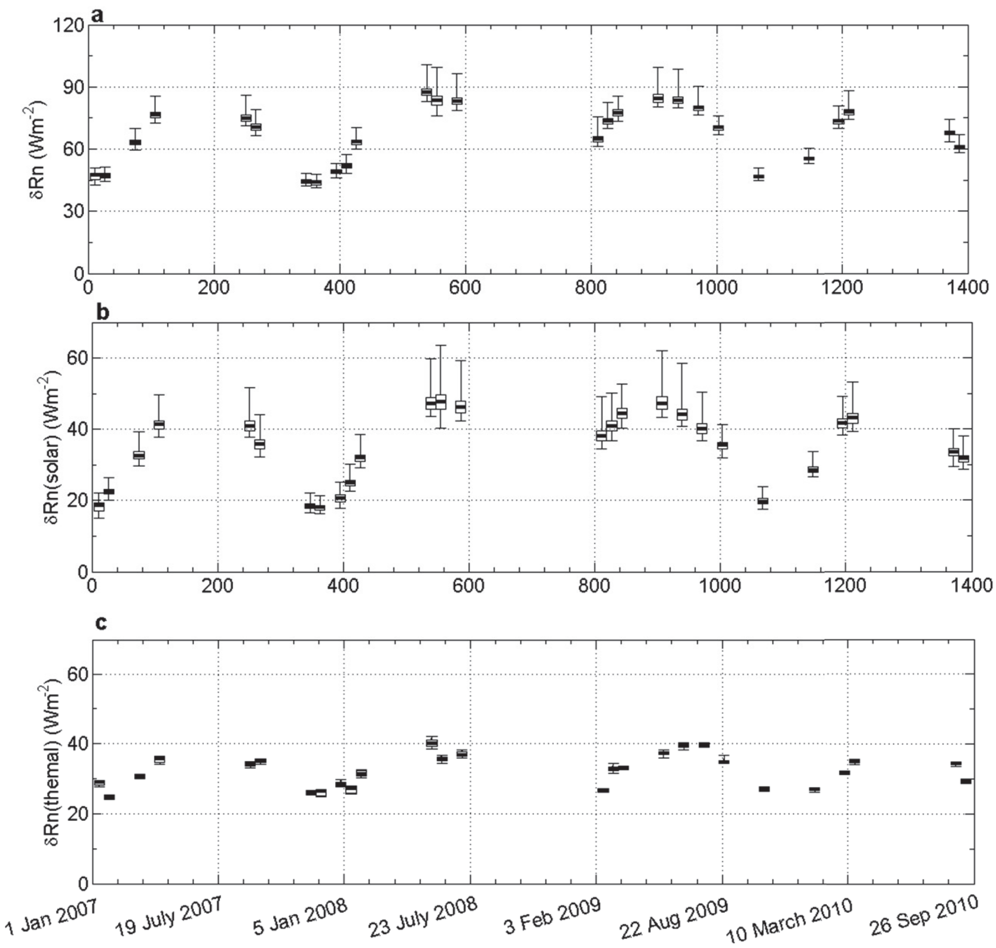

Fig. 8. Temporal variation of uncertainties in net radiation estimates using Landsat-7 data due to uncertainty in the most influencing factors. Global uncertainties in net radiation **(a)**, and corresponding uncertainty from the first term **(b)** and second term **(c)** of Eq. (1), followed by uncertainties in net radiation due to: 5% uncertainty in incoming solar irradiance **(d)**, 8% uncertainty in atmospheric irradiance **(e)**, and uncertainties in albedo from consideration of models *m1-m13* **(f)** or unbiased models *m2, m3, m8* and *m10* **(g)**. Uncertainties from **a** and **b** were computed considering unbiased albedo models *m2*, *m3*, *m8* and *m10*. Each boxplot belongs to an acquisition day and comprises the median (*i.e.*, central thick line), the first and third quartile (*i.e.*, inferior and superior edges of the boxes), and the extreme values excluding outliers (*i.e.*, inferior and superior whiskers).

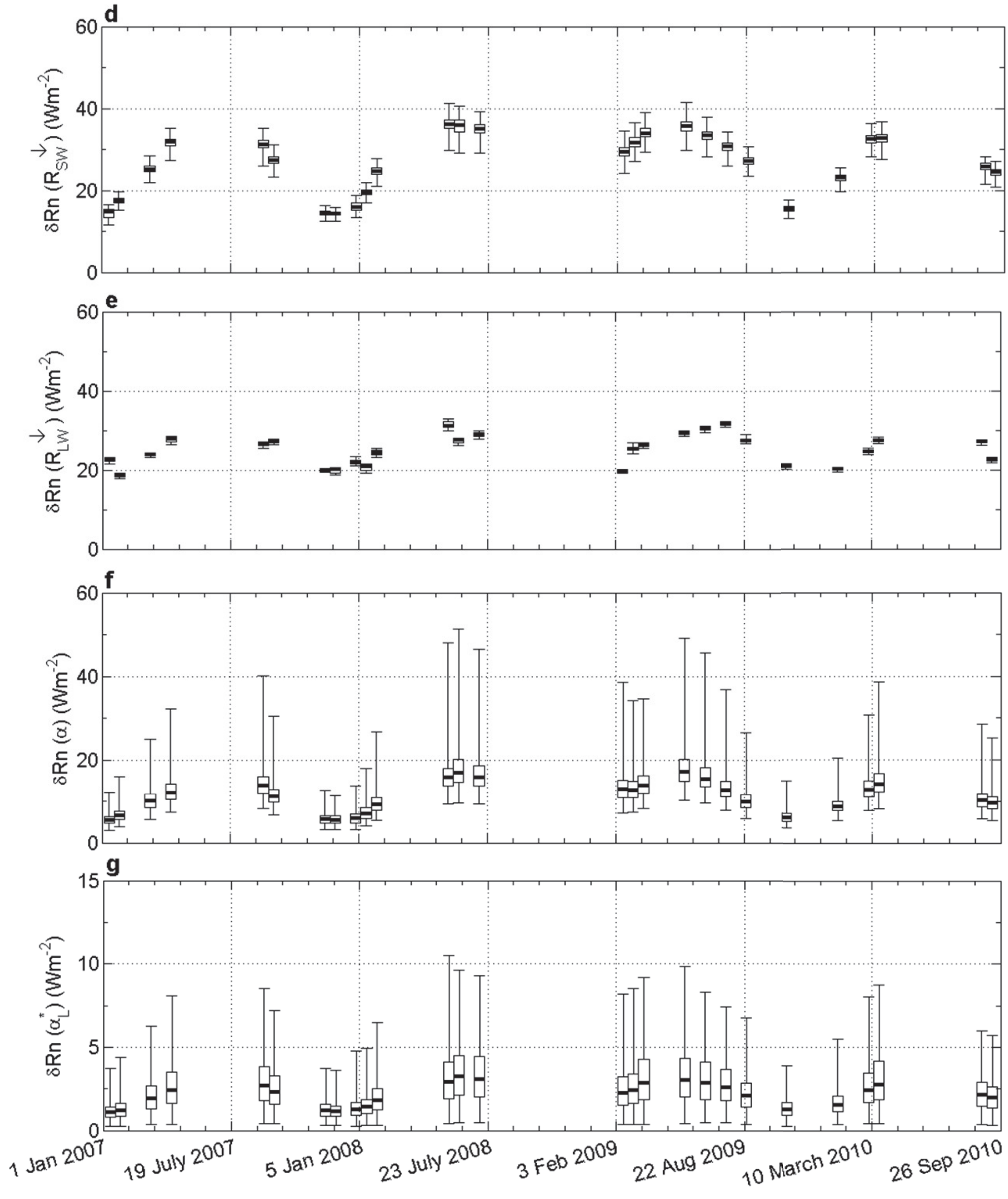

Continuation of Fig. 8

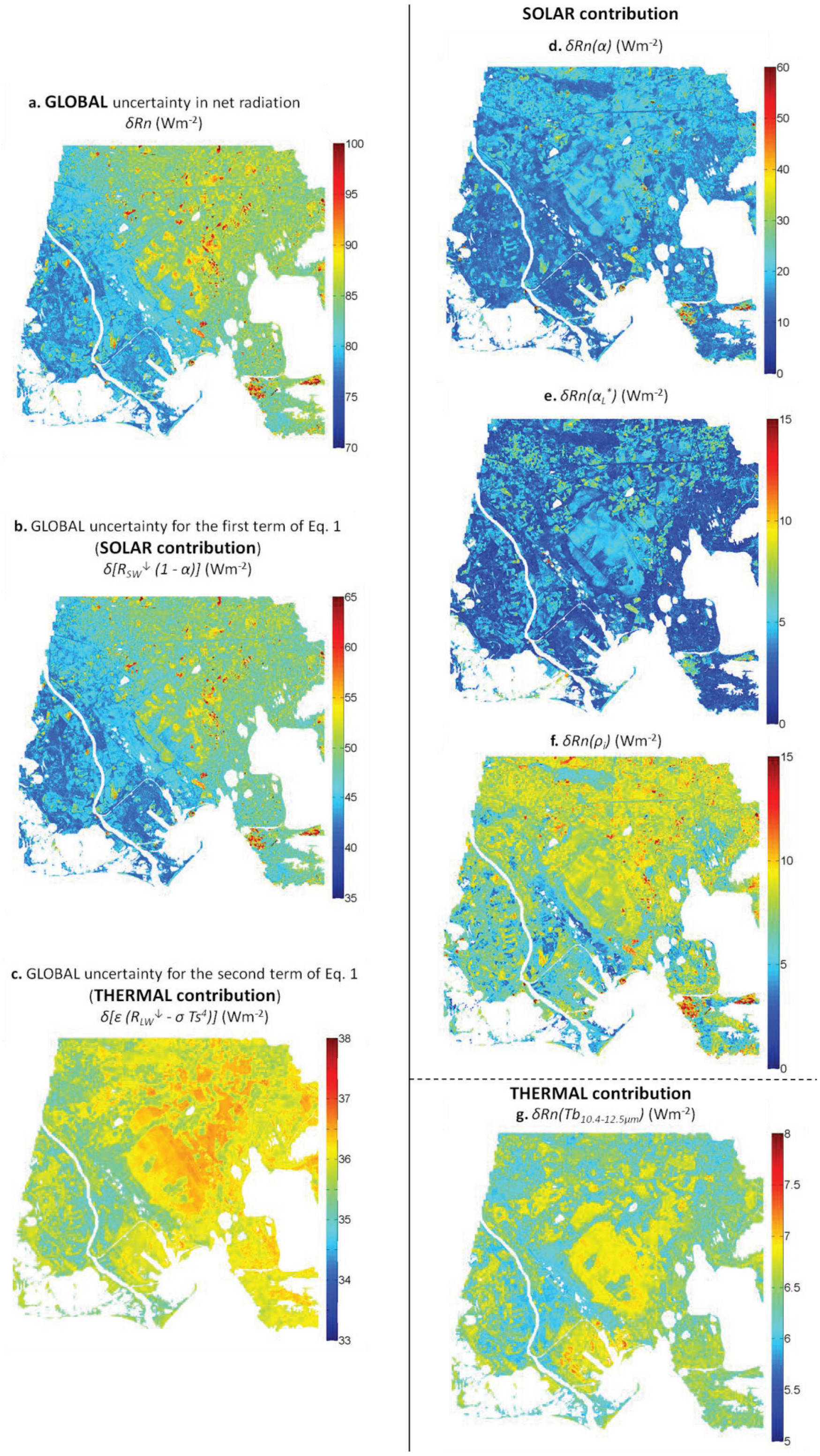

Fig. 9 (see below)

Fig. 9. Spatial distribution of uncertainties in net radiation estimates using Landsat-7 data (acquired at 10:30 UTC on July 8th, 2008 over the Crau-Camargue) due to uncertainty in the most influencing factors. Global uncertainties in net radiation **(a)**, and corresponding uncertainty from the first term **(b)** and second term **(c)** of Eq. (1), followed by uncertainties in net radiation due to: uncertainties in albedo from consideration of models *m1-m13* **(d)** or unbiased models *m2, m3, m8* and *m10* **(e)**, 5% uncertainty in spectral reflectances **(f)**, and 1 K uncertainty in brightness temperature **(g)**. Uncertainties from **a** and **b** were computed considering unbiased albedo models *m2*, *m3*, *m8* and *m10*. Pixels with value higher than the maximum (or lower than the minimum) value in the corresponding scale (*i.e.*, a small percentage of the entire image) are masked in red (or blue). Water, clouds, shadows, and pixels with an altitude higher than 100 m are masked in white.

TABLES

Table 1. Coefficients sets used to compute albedo as a linear combination of waveband Landsat-7 reflectances using Eq. (2), where *βo* is the offset and *Sensor* indicates the sensor for which each model was originally defined. Symbol "–" means that the band was not considered in the analysis; *bi* is the spectral band *i* from Landsat-7; *mj*: albedo model *j*; NIR: near infrared; MIR: middle infrared; TM: Thematic Mapper on board of Landsat-5; ETM+: Enhanced Thematic Mapper Plus on board of Landsat-7; MISR: Multi-angle Imaging Spectro Radiometer; AVHRR: Advanced Very High Resolution Radiometer; MSG: Meteosat Second Generation; MERIS: Medium Resolution Imaging Spectrometer.

Albedo model	Sensor	*Blue (b1)*	*Green (b2)*	*Red (b3)*	*NIR (b4)*	*MIR_1 (b5)*	*MIR_2 (b7)*	β_0
(m1) Bsaibes et al. (2009)	Formosat-2	–	–	0.619	0.402	–	–	–
(m2) Dubayah (1992)	TM	0.221	0.162	0.102	0.354	0.059	0.019	–
(m3) Duguay & Ledrew (1992)	TM	–	0.526	–	0.314	–	0.112	–
(m4) Jacob & Olioso (2002) – I	Airborne Polder	–	–	0.227	0.305	–	–	0.059
(m5) Jacob & Olioso (2002) – II		–	-0.136	0.334	0.316	–	–	0.059
(m6) Jacob & Olioso (2002) – III		-0.099	-0.087	0.351	0.314	–	–	0.058
(m7) Jacob & Olioso (2002) – IV		–	–	0.591	0.374	–	–	-0.001
(m8) Liang (2000)	TM/ETM+	0.356	–	0.130	0.373	0.085	0.072	-0.0018
(m9) Liang (2000)	MISR	–	0.126	0.343	0.415	–	–	0.004
(m10) Tasumi et al. (2008)	TM/ETM+	0.254	0.149	0.147	0.311	0.103	0.036	–
(m11) Weiss et al. (1999) – I	AVHRR	–	–	0.570	0.460	–	–	–
(m12) Weiss et al. (1999) – II	MSG-SEVIRI	–	0.680	0.080	0.350	–	–	–
(m13) Weiss et al. (1999) – III		0.06	0.69	0.001	0.35	–	–	–

Table 2. Spectral emissivities for bare soils and dense plant canopies measured *in situ* in La Crau area and over the Alpilles-ReSeDA experimental site (a small agricultural area mid-way of the Crau-Camargue region and Avignon). *In situ* measurements acquired over well-developed crops from other Mediterranean areas are also presented (similar crops as in our test site). All these *in situ* measurements were obtained using the Box method (Rubio et al., 1997) and thermal radiometers.

Reference [experimental site]	**Sample type *'Original label'***	**Short band emissivities**		
BARE SOIL		$\varepsilon_{10.2-11.3\ \mu m}$	$\varepsilon_{11.5-12.4\ \mu m}$	$\varepsilon_{8.0-13.5\ \mu m}$
Coll et al. (2002) [Alpilles]	*'101'*	0.962 ± 0.003	0.963 ± 0.004	0.961 ± 0.004
	'102'	0.967 ± 0.003	0.968 ± 0.003	0.968 ± 0.002
	'120'	0.963 ± 0.004	0.964 ± 0.004	0.965 ± 0.002
	'121'	0.967 ± 0.003	0.971 ± 0.005	0.967 ± 0.003
	'304'	0.962 ± 0.006	0.964 ± 0.005	0.963 ± 0.003
Coll et al. (2001) [Alpilles]	*'214'*			0.955 ± 0.018
	'500'			0.958 ± 0.013
	'Le Mas Neuf' – wet soil			0.979 ± 0.006
Labed and Stoll (1991) [La Crau]	Center of La Crau – soil without stones			0.9690 ± 0.0013
	Center of La Crau – dry stony area			0.959 ± 0.008
DENSE VEGETATION				$\varepsilon_{8.0-13.5\ \mu m}$
Coll et al. (2001) [Alpilles]	*'101'* Wheat (plant + soil)			0.987 ± 0.008
	'120' Wheat (plant + soil)			0.987 ± 0.005
	'101' Wheat (soil + stubble)			0.961 ± 0.011
	'120' Wheat (soil + stubble)			0.957 ± 0.015
	'203' Alfalfa full cover (plant + soil)			0.987 ± 0.004
Labed and Stoll (1991) [La Crau]	La Crau, north – very short grass			0.979
	La Crau, north – tufts of grass			0.981
	La Crau, north – grassland			0.983
	La Crau, north – bushes			0.994
DENSE VEGETATION IN OTHER AREAS		$\varepsilon_{10.2-11.3\ \mu m}$	$\varepsilon_{11.5-12.4\ \mu m}$	$\varepsilon_{8.0-13.5\ \mu m}$
Coll et al. (2003) [Barrax]	*'A4'* Alfalfa	0.978 ± 0.009	0.981 ± 0.007	0.980 ± 0.006
Olioso et al. (2007) [Marrakech]	Wheat	0.976 ± 0.009	0.984 ± 0.006	0.981 ± 0.006
Coll et al. (2010) [Albufera de Valencia]	Rice	$\varepsilon_{10.4-12.5\ \mu m}$ = 0.983 ± 0.005		(0.980 to 0.985) ± 0.005

Table 3. Emissivities in 10.4-12.5 µm and 8.0-13.5 µm bands and *NDVI* of dry and wet bare soils calculated from the reflectance spectra measured by Lesaignoux et al. (2013). Wet samples had soil moisture up to 45%.

'Original label'	**Emissivity ($\varepsilon_{\lambda1\text{-}\lambda2}$)**				***NDVI***	
	10.4–12.5 µm		**8.0–13.5 µm**			
	dry	**wet**	**dry**	**wet**	**dry**	**wet**
AVIGNON SITE (*site 1*)						
'84Avignon'	0.967	0.975	0.957	0.970	0.103	0.118
CRAU AREA						
'13Crau1'	0.973	0.986	0.963	0.981	0.191	0.186
'13Crau2'	0.972	0.985	0.961	0.979	0.175	0.189
CAMARGUE AREA						
'30BleA'	0.967	0.980	0.961	0.975	0.126	0.122
'30BleB'	0.965	0.983	0.964	0.979	0.101	0.114
'30BleC'	0.971	0.982	0.962	0.978	0.101	0.131
'30LuzerneA'	0.968	0.981	0.958	0.976	0.114	0.171
'30LuzerneB'	0.967	0.980	0.959	0.974	0.130	0.156
'30LuzerneC'	0.967	0.978	0.964	0.972	0.148	0.168
'30PrairieA'	0.967	0.980	0.966	0.975	0.217	0.235
'30PrairieB'	0.969	0.981	0.968	0.977	0.257	0.318
'30PrairieC'	0.971	0.985	0.960	0.981	0.227	0.261
'30SolNuA'	0.966	0.981	0.961	0.976	0.088	0.094
'30SolNuB'	0.968	0.982	0.957	0.976	0.079	0.099
'30SolNuC'	0.964	0.977	0.958	0.970	0.098	0.125
'30SolNuLabA'	0.965	0.981	0.959	0.975	–	–
'30SolNuLabB'	0.965	0.981	0.958	0.975	0.109	0.158
'30SolNuLabC'	0.963	0.978	0.961	0.972	0.120	0.170
'30VigneA'	0.968	0.981	0.957	0.975	0.085	0.108
'30VigneB'	0.966	0.977	0.956	0.971	0.083	0.124
'30VigneC'	0.965	0.979	0.958	0.972	0.114	0.145

Table 4. Statistical metrics from the validation of Landsat-7 albedo (α) with ground measurements from all available sites and days, for each albedo model after and before unbiasing (i.e, offset coefficient recomputed: $\beta_0' = \beta_0 - ME$). *ME*: Bias; $RMSE_A$ and $RMSE_R$: absolute and relative Root Mean Square Errors.

	[Dataset size 63]				
	***Albedo* (α)**			***Unbiased albedo* (α*) [*ME* = 0.000]**	
Albedo model	***ME***	$RMSE_A$	$RMSE_R$ **(%)**	$RMSE_A$	$RMSE_R$ **(%)**
m1	-0.002	0.026	14.5	0.026	14.4
m2	-0.023	0.033	18.7	0.024	13.3
m3	-0.024	0.033	18.5	0.022	12.6
m4	-0.011	0.028	15.7	0.026	14.5
m5	-0.010	0.028	15.6	0.026	14.5
m6	-0.012	0.029	16.1	0.026	14.6
m7	-0.014	0.029	16.0	0.025	13.9
m8	-0.010	0.025	14.1	0.023	13.1
m9	-0.011	0.029	16.2	0.027	14.9
m10	-0.018	0.029	16.1	0.023	12.7
m11	0.009	0.029	16.3	0.028	15.6
m12	-0.008	0.026	14.3	0.024	13.7
m13	-0.011	0.027	14.9	0.024	13.6

Table 5. Statistical metrics from the validation of Landsat-7 surface temperature (*Ts*) with ground measurements from all available sites and days. Calculations were performed using emissivity ($\varepsilon_{10.4\text{-}12.5\mu m}$) defined by *Curve A*, *Curve B* or *Curve C* (see Fig. 3). *ME*: Bias; $RMSE_A$: absolute Root Mean Square Error.

		Surface temperature (Ts)		
Sites	$\varepsilon_{10.4\text{-}12.5\mu m}$	***ME* (K)**	**$RMSE_A$ (K)**	**Dataset size**
All sites	*Curve A*	0.6	1.8	59
All sites	*Curve B*	0.3	1.7	59
All sites, except *Avignon*	*Curve B*	0.9	1.5	37
(1) Avignon site	*Curve B*	-0.08	2.2	22
(2) Coussouls site	*Curve B*	0.9	1.2	4
(3) Domaine du Merle site	*Curve B*	0.5	0.9	12
(4) Tour du Valat site	*Curve B*	0.5	1.6	21
All sites	*Curve C*	-0.14	1.7	59

Table 6. Statistical metrics from the validation of Landsat-7 net radiation (*Rn*) with ground measurements from all available sites and days, for each albedo model after and before unbiasing (i.e, offset coefficient recomputed: $\beta_0' = \beta_0 - ME$). *ME*: Bias; $RMSE_A$ and $RMSE_R$: absolute and relative Root Mean Square Errors.

***Net radiation* (*Rn*, W·m^{-2}) [Dataset size 62]**						
Albedo model	***Albedo* (*α*)**			***Unbiased albedo* (*α**)**		
	ME	***$RMSE_A$***	***$RMSE_R$* (%)**	***ME***	***$RMSE_A$***	***$RMSE_R$* (%)**
m1	-1.3	18.6	4.4	-2.7	18.9	4.5
m2	13.7	21.8	5.1	-1.7	18.4	4.3
m3	14.4	21.8	5.1	-1.5	17.6	4.1
m4	6.1	21.0	5.0	-0.9	20.6	4.9
m5	5.7	20.7	4.9	-1.0	20.4	4.8
m6	6.9	20.9	4.9	-1.0	20.4	4.8
m7	6.8	18.6	4.4	-2.4	18.5	4.4
m8	4.6	17.6	4.2	-1.7	17.7	4.2
m9	5.1	19.4	4.6	-2.4	19.6	4.6
m10	10.0	19.2	4.5	-1.6	17.4	4.1
m11	-8.9	22.4	5.3	-3.2	20.1	4.7
m12	2.9	18.0	4.2	-2.2	18.4	4.3
m13	5.2	18.4	4.3	-3.0	20.0	4.7

Table 7. Overview of global uncertainty (δ) in net radiation estimates using Landsat-7 data (in bold) and contribution from each term of Eq. (1). Details on uncertainties in net radiation (4th column) and uncertainties in intermediate variables (3rd column) due to uncertainty in one or several inputs (indicated in columns 2nd and 3rd). Three values are indicated, generally showing the lowest (29th Dec, 2007), mean (of values from the 29 days) and highest (8th July, 2008) uncertainty (by considering the median value of each image).

(see next page)

Inputs	Uncertainty in inputs	Median uncertainties in intermediate variables [Dec –(mean)– July]		Median uncertainties in Rn (Wm^{-2}) [Dec –(mean)– July]	
GLOBAL uncertainty in net radiation, δRn					**44 –(68)– 83**
GLOBAL uncertainty for the first term of Eq. 1 (SOLAR contribution), $\delta[R_{SW}^{\downarrow} (1 - \alpha)]$					18 –(35)– 48
$R_{SW}^{\downarrow}$	$\delta R_{SW}^{\downarrow} = 0.05\ R_{SW}^{\downarrow}$	$\delta R_{SW}^{\downarrow}$ =	17 –(32)– 44 Wm^{-2}	$\delta Rn(R_{SW}^{\downarrow})$ =	14 –(27)– 36
ρ_i	$\delta\rho_i = 0.05\ \rho_i$	$\delta\alpha_{m3*}(\rho_i)$ =	0.006 –(0.008)– 0.009	$\delta Rn(\rho_i)$ =	2 –(5)– 8
α	*models* = *m1-m13*	$\delta\alpha$ =	0.017 –(0.017)– 0.019	$\delta Rn(\alpha)$ =	6 – (11)– 17
	models = $m1^*$-$m13^*$	$\delta\alpha$ =	0.013 –(0.011)– 0.010	$\delta Rn(\alpha)$ =	4 –(7)– 9
	models = $m2^*$, $m3^*$, $m8^*$, $m10^*$	$\delta\alpha$ =	0.003 –(0.003)– 0.004	$\delta Rn(\alpha)$ =	1 –(2)– 3
	models = $m1^*$, $m2^*$, $m3^*$, $m8^*$, $m10^*$	$\delta\alpha$ =	0.005 –(0.005)– 0.005	$\delta Rn(\alpha)$ =	2 –(3)– 5
GLOBAL uncertainty for the second term of Eq. 1 (THERMAL contribution), $\delta[\varepsilon\ (R_{LW}^{\downarrow} - \sigma\ Ts^4)]$					26 –(32)– 36
$R_{LW}^{\downarrow}$	$\delta R_{LW}^{\downarrow} = 0.08\ R_{LW}^{\downarrow}$	$\delta R_{LW}^{\downarrow}$ =	21 –(26)– 28 Wm^{-2}	$\delta Rn(R_{LW}^{\downarrow})$ =	20 –(25)– 28
$Tb_{10.4\text{-}12.5\mu m}$	$\delta Tb_{10.4\text{-}12.5\mu m}$ = 1.0 K	$\delta Ts(Tb_{10.4\text{-}12.5\mu m})$ =	1.01 –(1.01)– 1.01 K	$\delta Rn(Tb_{10.4\text{-}12.5\mu m})$ =	5 –(6)– 6
$\varepsilon_{8.0\text{-}13.5\mu m}$	*models* = *Curve A*, *Curve C*	$\delta\varepsilon_{8.0\text{-}13.5\mu m}$ =	0.010 –(0.009)– 0.009	$\delta Rn(\varepsilon_{8.0\text{-}13.5\mu m})$ =	1 –(1)– 1
$\varepsilon_{10.4\text{-}12.5\mu m}$	*models* = *Curve A*, *Curve C*	$\delta\varepsilon_{10.4\text{-}12.5\mu m}$ =	0.009 –(0.009)– 0.008	$\delta Rn(\varepsilon_{10.4\text{-}12.5\mu m})$ =	2 –(2)– 3
		$\delta Ts(\varepsilon_{10.4\text{-}12.5\mu m})$ =	0.36 –(0.37)– 0.43 K		
$R_{LW}^{\downarrow}{}_{10.4\text{-}12.5\mu m}$	*models* = different values for W, e_a, T_a	$\delta R_{LW}^{\downarrow}{}_{10.4\text{-}12.5\mu m}$ =	2.1 –(2.3)– 2.4 Wm^{-2}	$\delta Rn(R_{LW}^{\downarrow}{}_{10.4\text{-}12.5\mu m})$ =	0 –(0)– 0
		$\delta Ts(R_{LW}^{\downarrow}{}_{10.4\text{-}12.5\mu m})$ =	0.07 –(0.05)– 0.05 K		
$\varepsilon_{10.4\text{-}12.5\mu m}$, $R_{LW}^{\downarrow}{}_{10.4\text{-}12.5\mu m}$	*models* = *Curve A*, *Curve C*; *models* = different values for W, e_a, T_a	$\delta Ts(\varepsilon_{10.4\text{-}12.5\mu m}, R_{LW}^{\downarrow}{}_{10.4\text{-}12.5\mu m})$ =	0.43 –(0.42)– 0.47 K	$\delta Rn(\varepsilon_{10.4\text{-}12.5\mu m}, R_{LW}^{\downarrow}{}_{10.4\text{-}12.5\mu m})$ =	3 –(2)– 2

Rn: net radiation; $R_{SW}^{\downarrow}$: incoming solar irradiance; $R_{LW}^{\downarrow}$: atmospheric irradiance; ρ_i: spectral reflectances; α: albedo, where m_i refers to the different albedo models, and m_i^* stands for unbiased albedo; *Ts*: surface temperature; Tb_λ: top of canopy brightness temperature in the spectral band λ; ε_λ: emissivity in the spectral band λ; $R_{LW}^{\downarrow}{}_\lambda$: incoming atmospheric radiation in the spectral band λ; W: precipitable water content of the atmosphere; e_a: air water vapor pressure; T_a: air temperature; *Curve A* and *Curve C*: specified in Table 5 and Fig. 3.

1384 **Table 7**

Figure 1

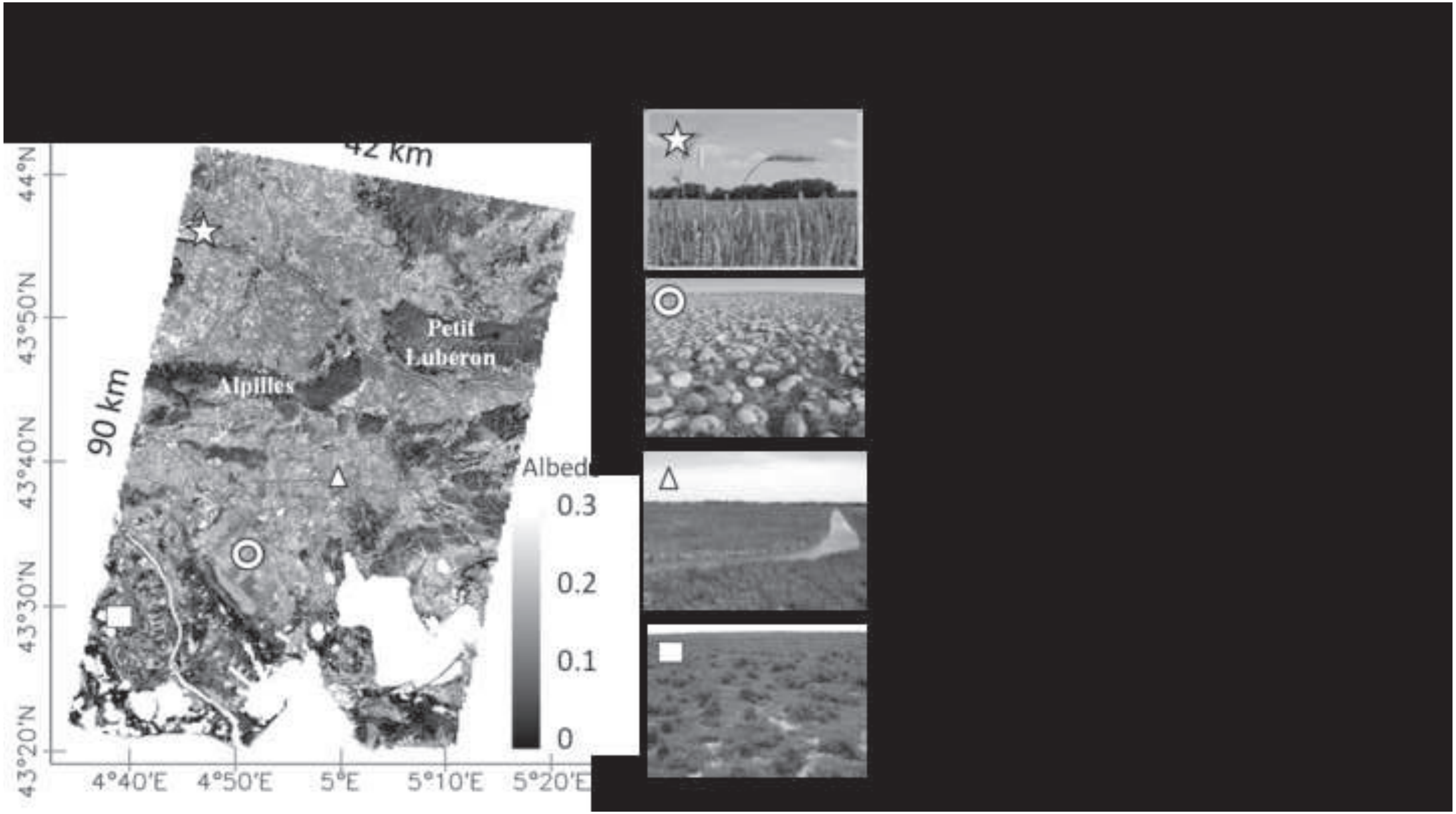
42 km
90 km
Petit
Luberon
Alpilles
Albedo
0.3
0.2
0.1
0
44°N
43°50'N
43°40'N
43°30'N
43°20'N
4°40'E
4°50'E
5°E
5°10'E
5°20'E

Figure 2

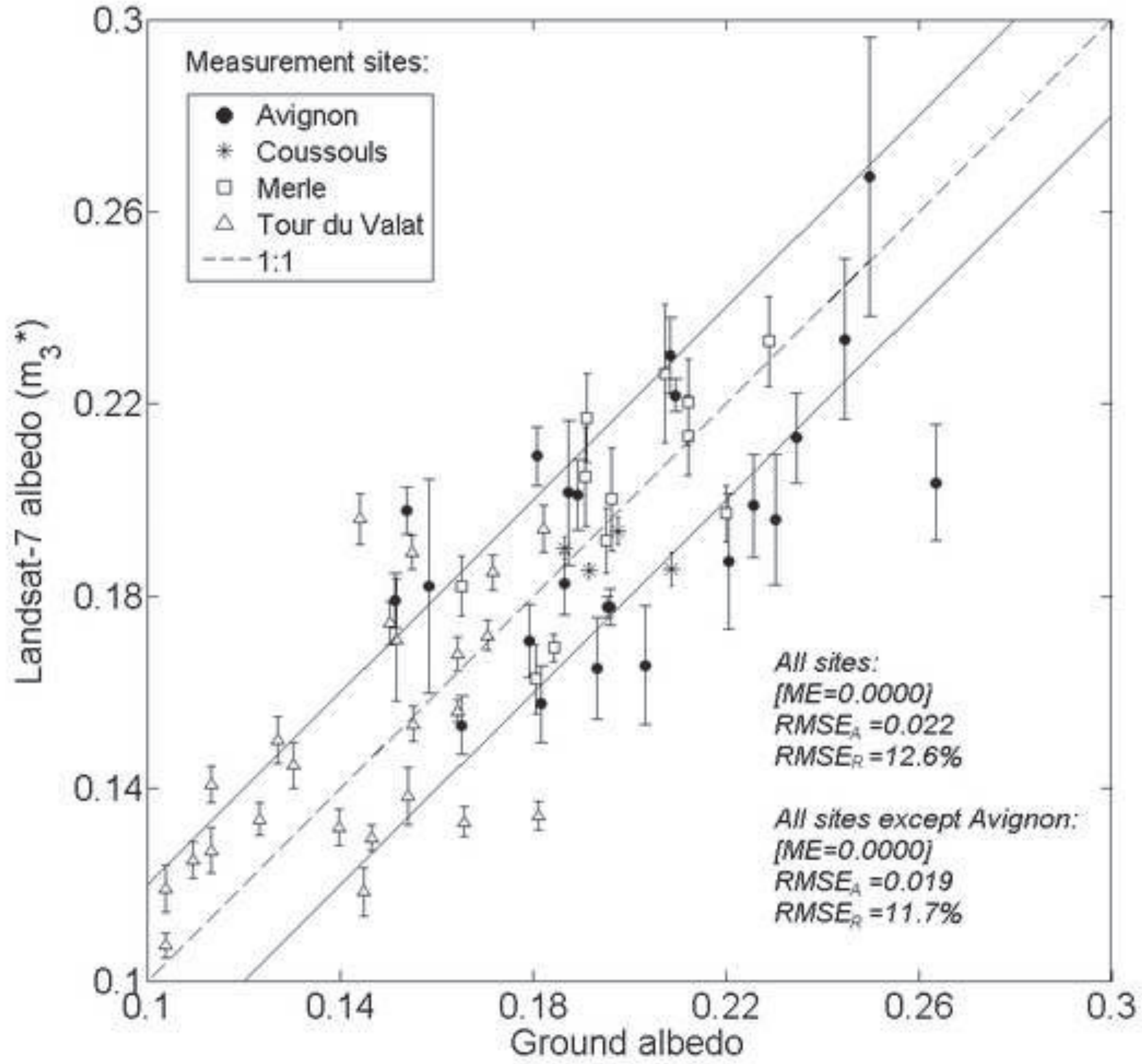
Measurement sites:
Avignon
Coussouls
Merle
Tour du Valat
1:1
0.3
0.26
0.22
0.18
0.14
0.1
Landsat-7 albedo (m_3*)
0.1
0.14
0.18
0.22
0.26
0.3
Ground albedo
All sites:
[ME=0.0000]
$RMSE_A$ =0.022
$RMSE_R$ =12.6%
All sites except Avignon:
[ME=0.0000]
$RMSE_A$ =0.019
$RMSE_R$ =11.7%

Figure 3a
Click here to download high resolution image

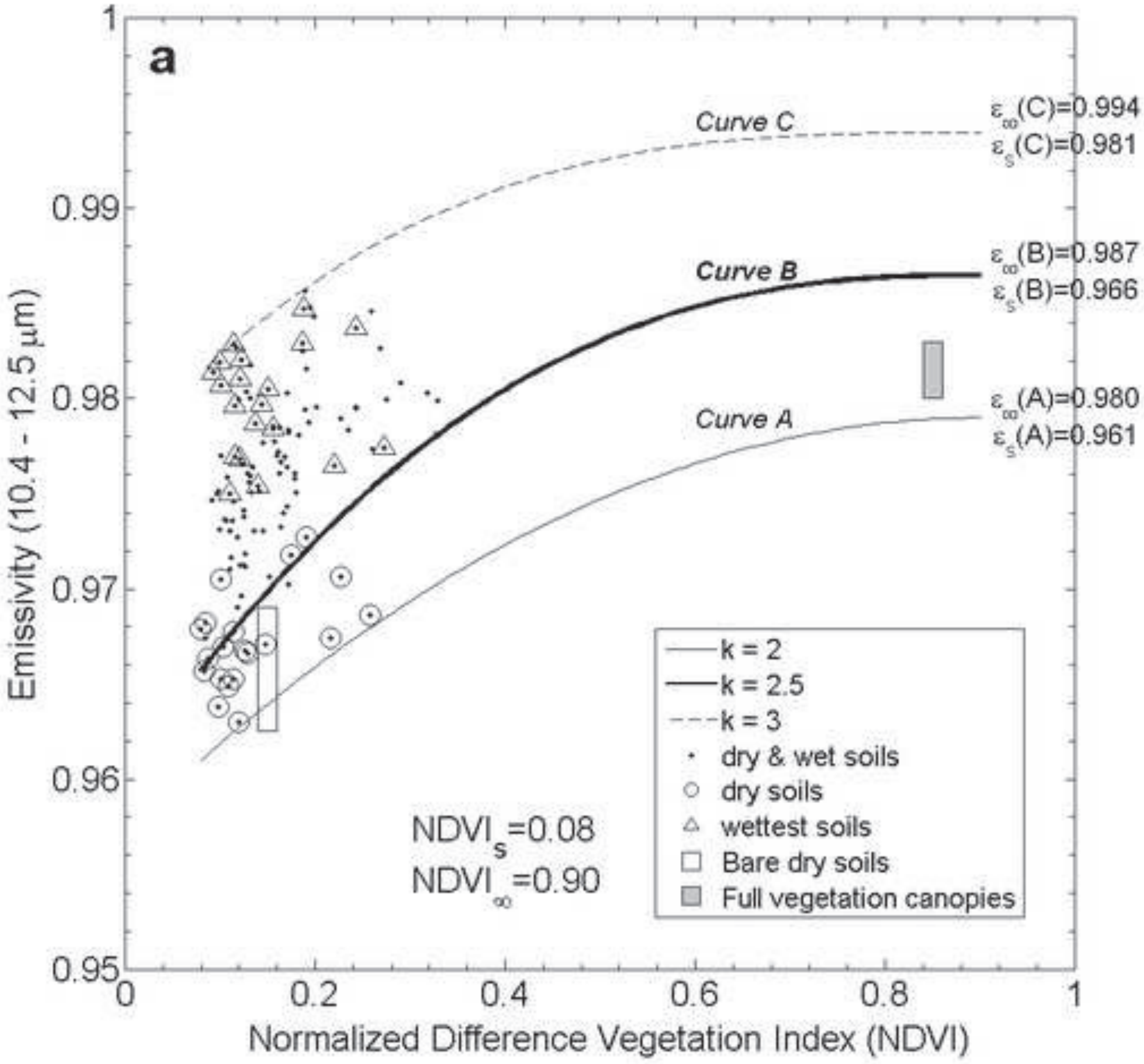

Figure 3b
Click here to download high resolution image

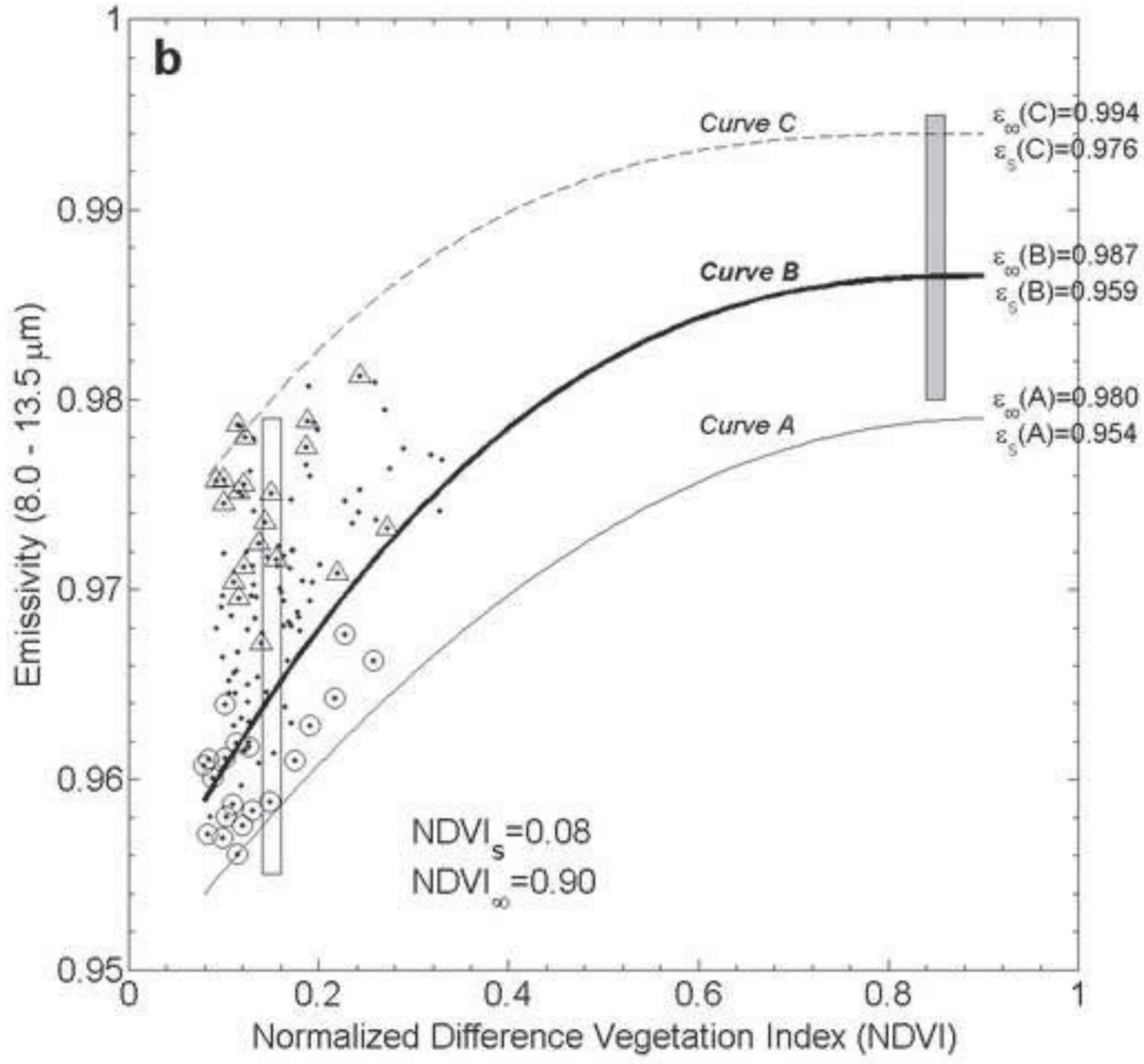

Figure 4

Click here to download high resolution image

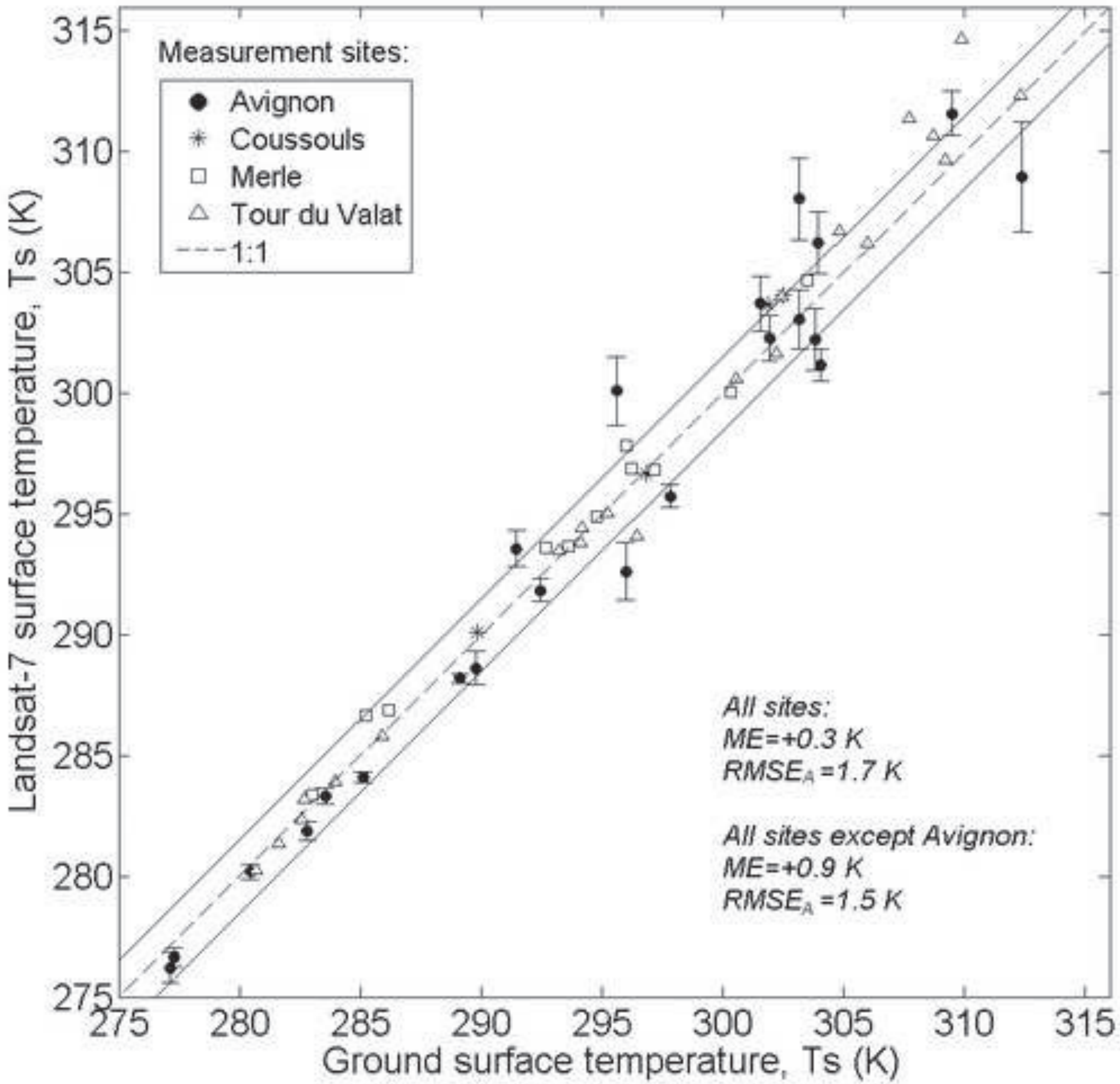

Figure 5

Click here to download high resolution image

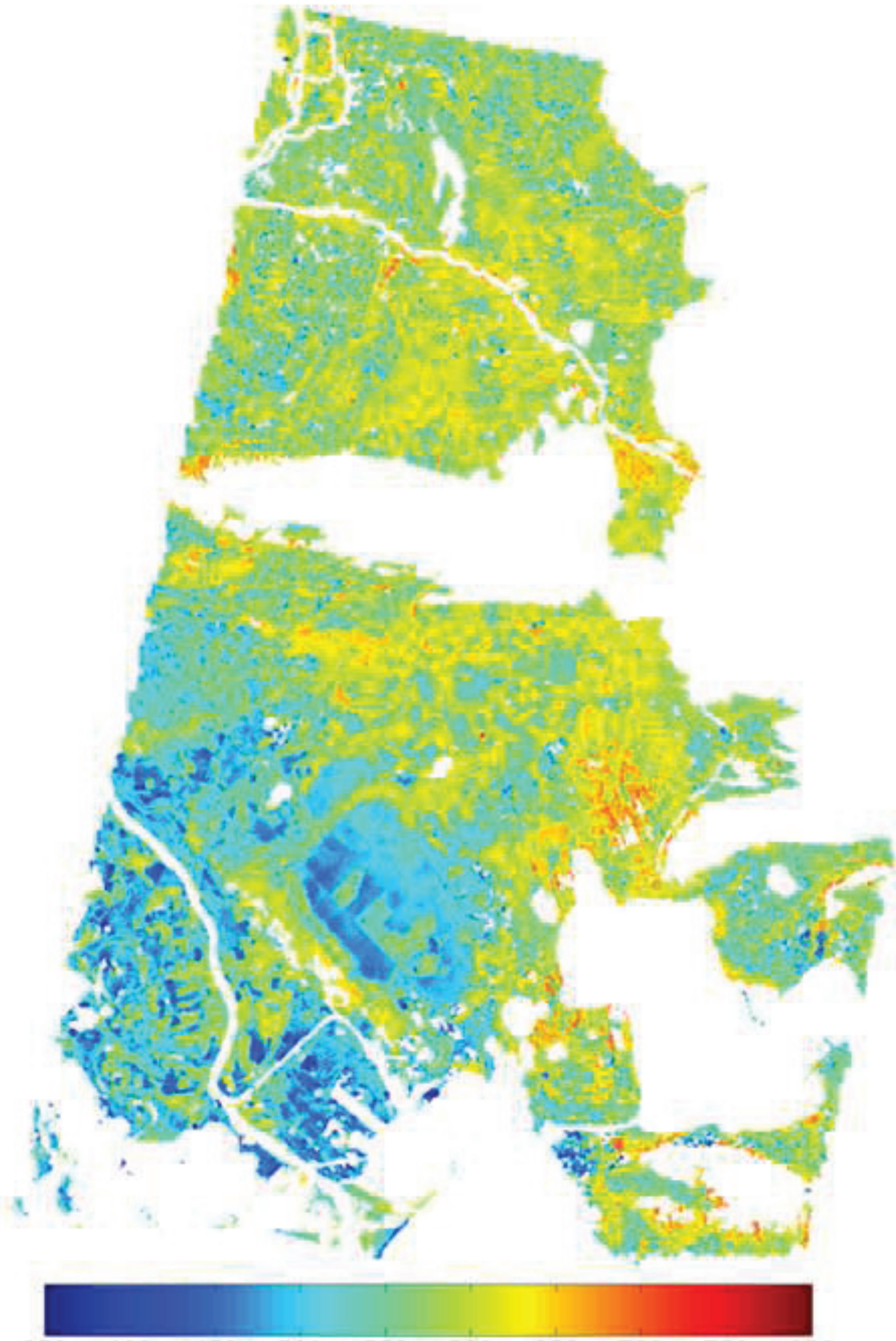

Figure 6

Click here to download high resolution image

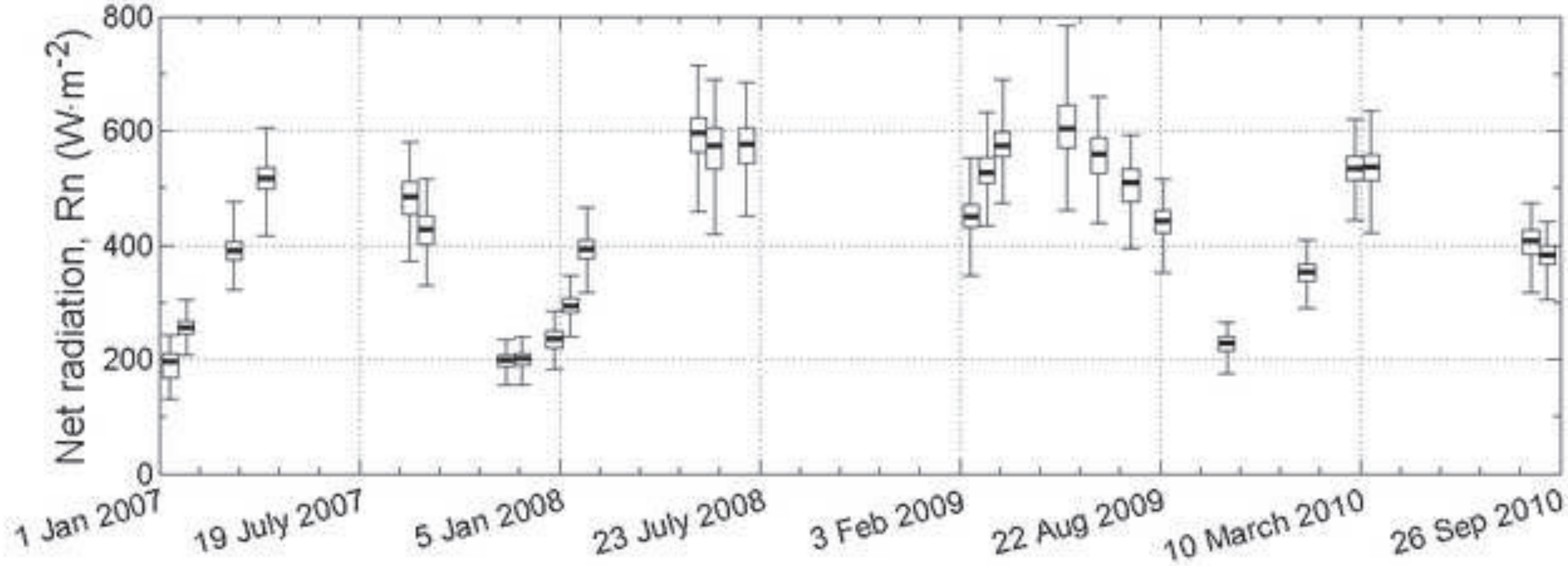

Figure 7

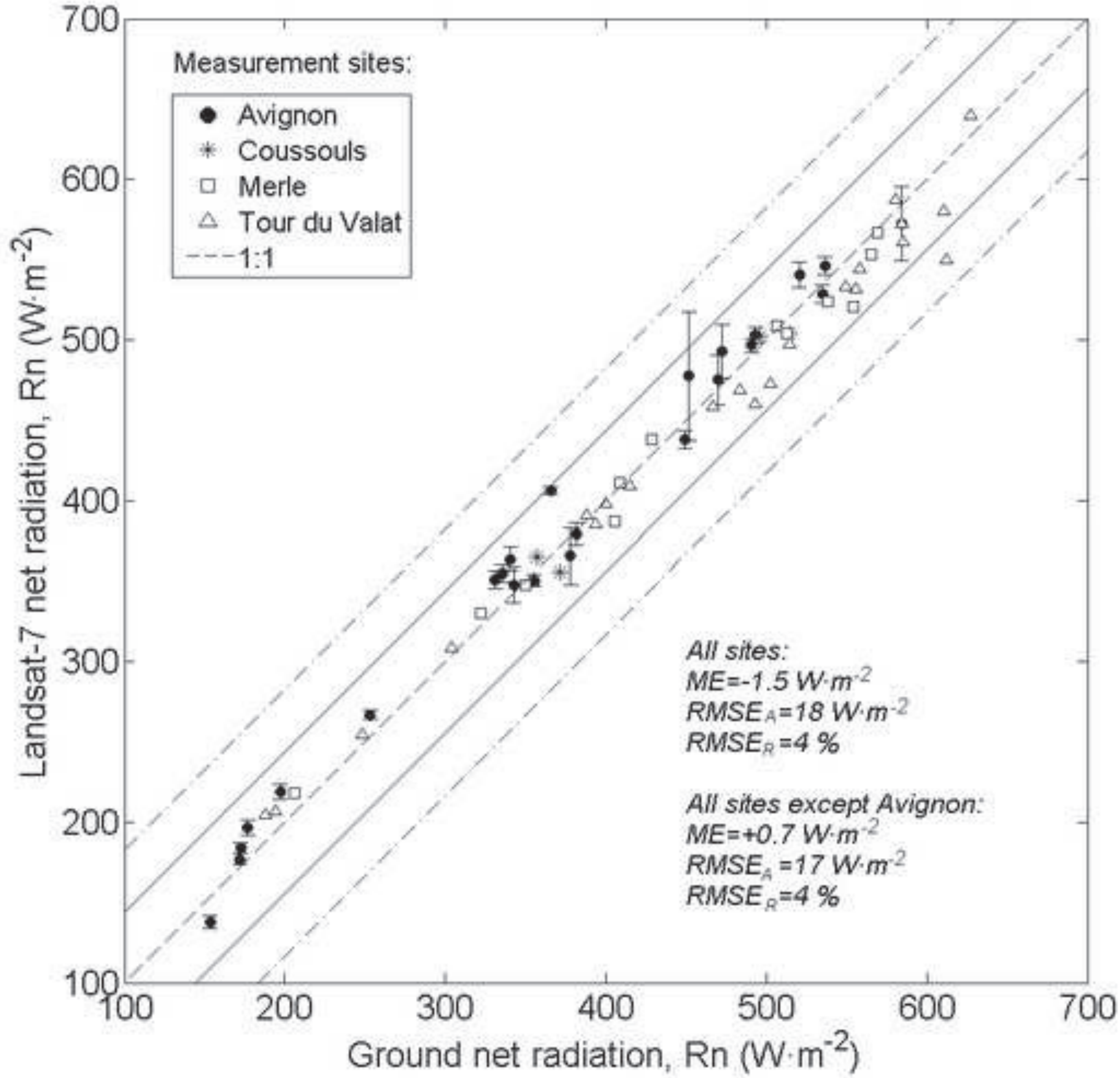

Measurement sites:
Avignon
Coussouls
Merle
Tour du Valat
1:1
All sites:
ME=-1.5 W·m^-2
RMSE_A=18 W·m^-2
RMSE_R=4 %
All sites except Avignon:
ME=+0.7 W·m^-2
RMSE_A=17 W·m^-2
RMSE_R=4 %
Landsat-7 net radiation, Rn (W·m^-2)
Ground net radiation, Rn (W·m^-2)
100
200
300
400
500
600
700

Figure 8A

Click here to download high resolution image

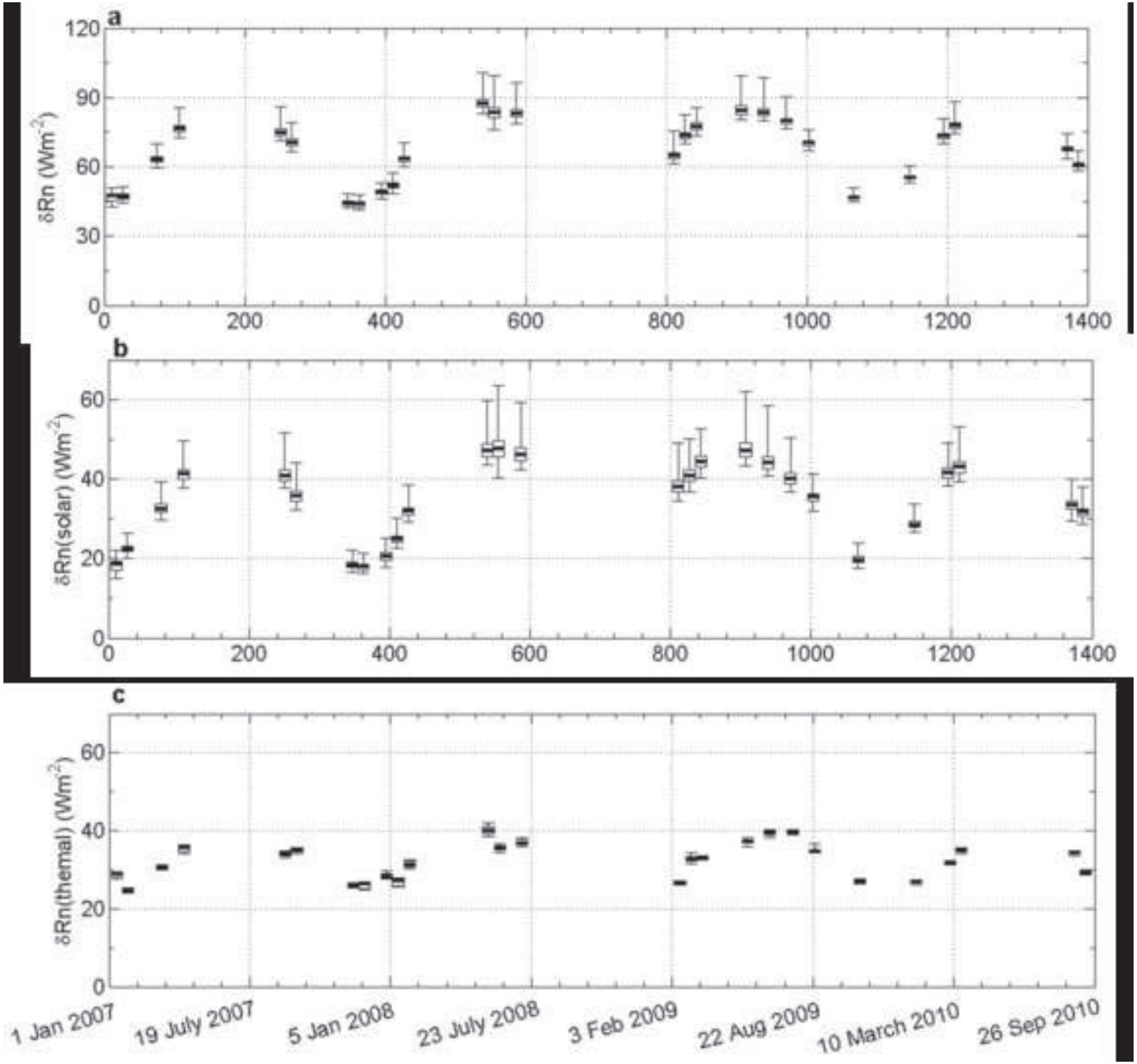

Figure 8B
Click here to download high resolution image

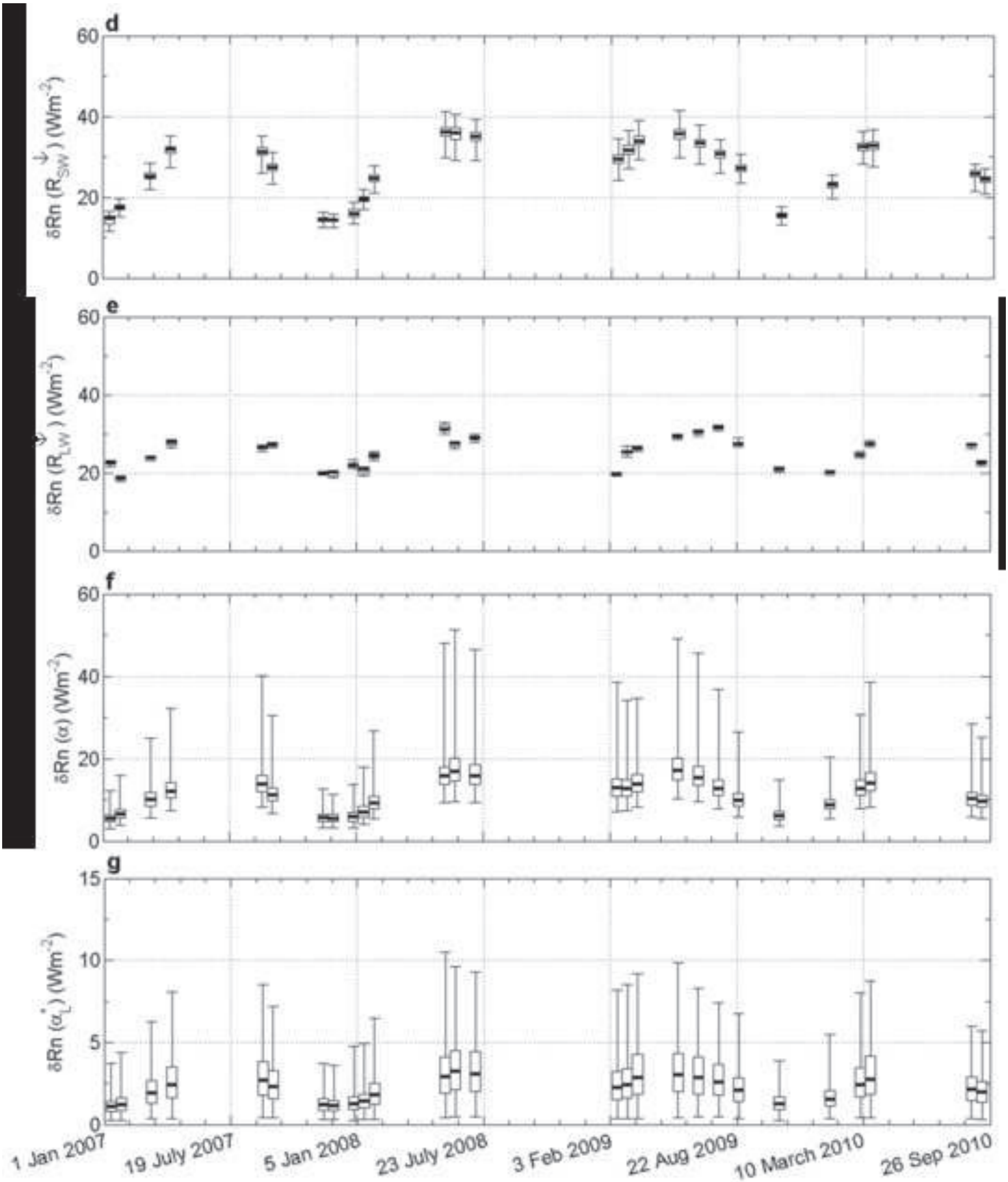

Figure 9
Click here to download high resolution image